

The incommensurately modulated structures (IMS) of low-temperature labradorite feldspars: a single-crystal X-ray and neutron diffraction study

Authors

Shiyun Jin^a, Huifang Xu^{a*}, Xiaoping Wang^b, Ryan Jacobs^c and Dane Morgan^c

^aDepartment of Geoscience, University of Wisconsin-Madison, 1215 W. Dayton Street, Madison, WI, 53706, USA

^bNeutron Scattering Division, Oak Ridge National Laboratory, P.O. Box 2008 MS-6475, Oak Ridge, TN, 37831, USA

^cDepartment of Materials Science and Engineering, University of Wisconsin-Madison, 1509 University Ave, Madison, WI, 53706, USA

Correspondence email: hfxu@geology.wisc.edu

Synopsis The puzzle of the complicated relations among composition, cooling rate and the incommensurate ordering of the plagioclase feldspar solid solution series is completed by filling in the structures of *e*-labradorite with incommensurate modulation as one of the last pieces.

Abstract Labradorite feldspars of the plagioclase solid solution series have been known for their complicated subsolidus phase relations and enigmatic incommensurately modulated structures. Characterized by the irrationally indexed *e*-reflections in the diffraction pattern, *e*-labradorite shows the largest variation in the incommensurate ordering states among the *e*-plagioclase structures. The strongly ordered low-temperature *e*-labradorite is one of the last missing pieces of the *e*-plagioclase puzzle. Nine plutonic and metamorphic labradorite feldspar samples from Canada, Ukraine, Minnesota (USA), Tanzania and Greenland with compositions ranging from An_{52.5} to An₆₈ were studied with single-crystal X-ray diffraction. Two crystals from Labrador, Canada, and Duluth, MN, USA, with wide enough twin lamellae were analyzed with single-crystal neutron diffraction. The incommensurately modulated structures of *e*-plagioclase are refined for the first time with neutron diffraction data, which confirmed that the T—O distance modulation in the low-temperature *e*-plagioclase results from the Al—Si ordering in the framework. Detailed configurations of the M site are also observed in the structures refined from neutron diffraction data, which were not possible to see with X-ray diffraction data. The relation between the **q**-vectors and the mole% An composition is revealed for the entire compositional range of *e*-plagioclase, from An₂₅ to An₇₅. The previously proposed two-trend relation depending on the cooling rate and phase transition path is confirmed. A new classification of *e*-plagioclase (e_α , e_β and e_γ)

IMPORTANT: this document contains embedded data - to preserve data integrity, please ensure where possible that the IUCr Word tools (available from <http://journals.iucr.org/services/docxtemplate/>) are installed when editing this document.

is proposed based on the \mathbf{q} -vector of the structure, which makes it an independent character from the presence/absence of density modulation. New parameters are proposed to quantify the ordering states of these complicated aperiodic structures of *e*-plagioclases, such as the difference between $\langle T_{10}—O \rangle$ and $\langle T_{1m}—O \rangle$ at phase $t = 0.2$ or the normalized intensity of the $(071\bar{1})$ reflection.

Keywords: Labradorite; *e*-plagioclase; neutron diffraction; incommensurately modulated structure; density modulation.

1. Introduction

Labradorite, the intermediate to calcic member of the plagioclase solid solution series, is one of the most famous species of the feldspar group. It has a chemical formula of $\text{Ca}_x\text{Na}_{1-x}\text{Al}_{1+x}\text{Si}_{3-x}\text{O}_8$, with x between 0.5 and 0.7. Labradorites are most commonly found in mafic igneous rocks such as basalt and gabbro. They are also the main component of anorthosite, which are the intrusive rocks composed by more than 90% plagioclase. Labradorites are best known for their brilliant iridescent optical effect (also known as schiller), due to the semi-periodic, nano-scaled exsolution lamellae in the structure. The exsolution lamellae are the result of the phase separation in the Bøggild miscibility gap, which is one of the three miscibility gaps (peristerite, Bøggild and Huttenlocher) in the complete solid solution series between albite (Ab: $\text{NaAlSi}_3\text{O}_8$) and anorthite (An: $\text{CaAl}_2\text{Si}_2\text{O}_8$) (Ribbe, 1983).

The subsolidus phase relations of the plagioclase solid solution series has been puzzling mineralogists and petrologists for decades, mainly due to the complexity introduced by the enigmatic incommensurately modulated structures (IMS) that occur in the intermediate plagioclase ($\text{An}_{25}\sim\text{An}_{75}$) formed at low temperature. The IMS of low-temperature plagioclase are characterized by the satellite reflections (*e*-reflections) in the diffraction pattern, which cannot be indexed with integer Miller indices. Therefore, the plagioclase with incommensurate structures are also known as *e*-plagioclase. The *e*-plagioclase can be further divided into two different phases, *e*1 and *e*2, discerned by the appearance and absence of *f*-reflections (second-order satellites) in the diffraction pattern (Jin & Xu, 2017*c*), respectively. The phase relations within the labradorite composition are the most complicated part of the plagioclase solid solution series, with $C\bar{1}$ (high-albite structure), $I\bar{1}$ (anorthite structure) stable at high temperature and *e*1 stable at low temperature, along with *e*2 often occurring as a metastable structure. These complex phase relationships are a key reason why labradorite is the most studied species of the plagioclase feldspars.

Labradorites are ideal subjects for understanding the incommensurately modulated structures due to their sharp and strong yet nicely separated satellite peaks in the diffraction pattern. In fact, most of the single-crystal X-ray analyses of *e*-plagioclase were done on labradorites (Boysen & Kek, 2015; Jin & Xu, 2017*b,c*; Horst *et al.*, 1981; Yamamoto *et al.*, 1984; Toman & Frueh, 1973*a*, 1976*a,b*, 1971, 1972, 1973*b,c*). Jin & Xu (2017*b*) finally provided a detailed structural model supporting Xu's (2015) direct

observation through Z-contrast imaging with scanning transmission electron microscopy (STEM). By comparing the structures of 11 andesine and oligoclase samples from both metamorphic and igneous rocks, the phase relation between $e1$, $e2$ and $C\bar{1}$ is constrained for the Na-rich compositions (Jin & Xu, 2017a). More recent studies on basalt phenocryst (Jin, Wang *et al.*, 2018; Jin, Xu *et al.*, 2019) and anorthosite xenolith (Jin, Wang *et al.*, 2018) clarified the phase relations of labradorite at high temperature. However, there are still several unanswered questions about the labradorite section of the phase diagram, such as the relation between $I\bar{1}$ structures and $e1$ structures, and how the thermal history of the host rock affects the ordering states of e -plagioclase. In this work, we selected e -labradorite samples with various compositions and thermal histories, and combined single-crystal X-ray and neutron diffraction to form a more complete understanding of the behavior of the e -plagioclase phase in this solid solution series.

2. Sample and experiment

Nine plutonic and metamorphic plagioclase samples from Canada, Ukraine, Minnesota, Tanzania and Greenland were studied in this work. The compositions, localities, brief descriptions and some references are listed in Table 1. All of the samples show dense albite-twin lamellae, and the single crystals for X-ray diffraction are picked from either thin sections or crushed pieces. Sample 7147A and Dul-15-6A are the only two with wide enough twin lamellae (up to ~ 2 mm) for single-crystal neutron diffraction. $1.5\text{mm} \times 2\text{mm} \times 2.5\text{mm}$ blocks are cut from individual twin lamellae along the (010), (001), and (40 $\bar{3}$) (approximately perpendicular to the a -axis) planes for neutron diffraction experiment. The chemical compositions of the samples were analysed with a CAMECA SXFive field emission electron microprobe at 15kV and 10nA beam current with a 20- μm beam size. Plagioclase and iron oxide standards were used in the microprobe analysis, and the results are listed in Table S1.

The complete X-ray diffraction data were collected on a Bruker Quazar APEXII single-crystal diffractometer with $\text{MoK}\alpha$ $I\mu\text{S}$ source and APEX2 detector. Different scan width and exposure time were planned for each data set depending on the different separations of the satellite peaks in each sample. The instrument was run at a voltage and current of 50 kV and 0.6 mA, respectively. Unit-cell parameters were calculated and refined using APEX3 software. The single-crystal neutron diffraction data were collected at BL-12 (TOPAZ) of Spallation Neutron Source (SNS) at Oak Ridge National Laboratory. Data collection strategy was calculated and optimized with the *CrystalPlan* software (Zikovskiy *et al.*, 2011) using the orientation matrix obtained from the initial sample orientation. Data sets with more than 95% completeness with resolution of 0.5 \AA were collected. Detected neutrons are stored as events with associated time of detection, detector and pixel information. Data were displayed, auto-indexed and integrated using the suite of algorithms in *Mantid* (Arnold *et al.*, 2014). These events were transformed into Q-space and integrated using a 3-D ellipsoid fitted to each reflection in accordance with previously reported methods (Schultz *et al.*, 2014). The integrated intensities were then

scaled and corrected for detector efficiency, the spectrum of the incident beam and Lorentz factors with the *ANVRED3* program (Schultz *et al.*, 1984). Absorption corrections, assuming spherical samples were also applied in *ANVRED3*. Both the X-ray and neutron diffraction data were collected at 100K.

The refinement of the structures was carried out with JANA2006 (Petříček *et al.*, 2014) on F^2 . For purposes of comparison, structure refinement with neutron data was also done using the cell parameters from X-ray diffraction, since the results of the cell parameters from X-ray diffraction are much more accurate with smaller crystal and beam size compared to neutron diffraction. The 3D crystal structure was visualized by VESTA (Momma & Izumi, 2011). The lattice parameters of the samples and some details of data and structure refinements are listed in Table 2.

Table 1 Compositions, provenance, and structural states of the samples used in this study

Sample	Composition	Locality	Description	Structure	References
7147A	An _{52.5}	Labrador, Canada	iridescent crystal from anorthosite, crystal size up to ~15cm. Cloudy grey color	sharp <i>e&f</i>	McLaren, 1974
Volga Blue yellow	An ₅₅	Zhitomir Province,	iridescent anorthosite, crystal size up to ~5cm, dark grey. No iridescent color at core or rim, blue to yellow iridescent color in the middle	sharp <i>e&f</i>	Bogdanova <i>et al.</i> , 2004
Volga Blue colorless	An ₅₉	Ukraine			
89GM97	An ₅₇	Duluth, Minnesota, USA	troctolite in the Duluth igneous complex, dark grey color	sharp <i>e&f</i>	Carpenter & McConnell, 1984; Carpenter, 1986
67796b	An ₆₀	Gulela Hills, Tanzania	Anorthositic granulite	sharp <i>e&f</i>	Carpenter <i>et al.</i> , 1985
11044.p1	An ₆₀	Duluth, Minnesota, USA	Anorthosite	sharp <i>e&f</i>	Carpenter & McConnell, 1984; Carpenter <i>et al.</i> , 1985; Carpenter, 1986
Dul-15-6A	An ₆₄	Duluth, Minnesota, USA	Anorthosite xenolith in Duluth complex, clear light green color	sharp <i>e&f</i>	Miller & Weiblen, 1990; Miller, 2009
SKHHM	An ₆₇	Skaergaard, Greenland	Gabbro, Hidden Zone	sharp <i>e&f</i>	Carpenter <i>et al.</i> , 1985; Carpenter, 1986
11044.p3	An ₆₈	Duluth, Minnesota, USA	Anorthosite	sharp <i>e</i> , no <i>f</i>	Carpenter, 1986

Table 2 Experimental details of single-crystal X-ray and neutron diffraction

	7147A	7147A neutron	Volga Blue yellow	89GM97	Volga Blue colourless	11044.p1	67796b	Dul-15-6A	Dul-15-6A neutron	SKHHM	11044.p3
Crystal data											
Chemical formula	Ca _{0.525} Na _{0.475} Al _{1.525} Si _{2.475} O ₈	Ca _{0.892} Al _{1.525} Si _{2.475} O ₈	Ca _{0.55} Na _{0.45} Al _{1.55} Si _{2.45} O ₈	Ca _{0.57} Na _{0.43} Al _{1.57} Si _{2.43} O ₈	Ca _{0.59} Na _{0.41} Al _{1.59} Si _{2.41} O ₈	Ca _{0.6} Na _{0.4} Al _{1.6} Si _{2.4} O ₈	Ca _{0.6} Na _{0.4} Al _{1.6} Si _{2.4} O ₈	Ca _{0.64} Na _{0.36} Al _{1.64} Si _{2.36} O ₈	Ca _{0.918} Al _{1.64} Si _{2.36} O ₈	Ca _{0.67} Na _{0.33} Al _{1.67} Si _{2.33} O ₈	Ca _{0.68} Na _{0.32} Al _{1.68} Si _{2.32} O ₈
<i>a</i> , <i>b</i> , <i>c</i> (Å)	8.1640 (3) 12.8534 (2) 14.2098 (4)		8.1690 (2)	8.1742 (3)	8.1729 (1)	8.1719 (2)	8.1652 (3)	8.1684 (3)		8.1809 (10)	8.1724 (2)
<i>α</i> , <i>β</i> , <i>γ</i> (°)	93.6187 (11) 116.2531 (15) 89.781 (3)		93.6017 (7)	93.4852 (11)	93.5722 (5)	93.5140 (7)	93.5933 (9)	93.5396 (7)		93.5325 (15)	93.5256 (8)
<i>V</i> (Å ³)	1334.15 (7)		1334.56 (4)	1337.33 (7)	1336.51 (3)	1335.89 (4)	1333.69 (7)	1335.59 (6)		1339.8 (2)	1336.04 (4)
Modulation Wave vectors	0.06747(2) 0.04777(4) -0.22896(4)		0.06026(6)	0.03569(6)	0.05247(5)	0.04870(4)	0.04877(6)	0.03882(3)		0.01745(4)	0.0312(3)
period (Å)	30.3		32.3	42.6	35.2	36.8	35.3	39.8		59.4	47.1
Crystal size (mm)	0.072×0.162 ×0.182	2×2×2	0.055×0.11 2×0.119	0.057×0.10 2×0.137	0.044×0.05 6×0.075	0.055×0.10 5×0.112	0.044×0.07 0×0.121	0.065×0.10 8×0.135	2×2×2	0.036×0.06 4×0.102	0.057×0.07 3×0.089
Data collection											
Distance	50mm	39-46cm	60mm	50mm	50mm	50mm	50mm	50mm	39-46cm	50mm	60mm
Exposure	90s/frame	13C/run	65s/frame	65s/frame	78s/frame	70s/frame	60s/frame	65s/frame	12C/run	60s/frame	60s/frame
Scanning width (°)	0.5°	N/A	0.5°	0.5°	0.5°	0.5°	0.5°	0.5°	N/A	0.7°	0.5°
Runs	4ω+1φ	23	7ω+1φ	3ω+1φ	3ω+1φ	3ω+1φ	4ω+1φ	4ω+2φ	28	3ω+1φ	8ω
Total	55048	45240	32770	32224	63069	32383	39876	53585	45606	25254	12177
Independent reflections	13929 (1876+4035+ 3974+4044) ^a	45240 ^b (14482+218 00+8958)	10151 (2031+40 74+4046)	10156 (2024+40 80+4052)	18772 (3741+75 24+7507)	10094 (2014+405 7+4023)	10151 (2033+407 3+4045)	12249 (2431+494 9+4869)	16387 (5314+804 4+3029)	6776 (1363+27 16+2697)	6115 (2039+40 76)
observed reflections	8414 (1851+3547 +2325+691)	38533 (13778+188 57+5898)	4654 (1809+24 40+405)	5174 (1869+25 69+736)	5597 (2483+26 72+442)	4867 (1829+254 8+490)	5543 (1842+275 0+951)	7543 (2272+361 6+1655)	14829 (5250+746 1+2118)	4330 (1281+19 89+1060)	3085 (1692+13 93)
<i>R</i> _{int}	0.067	N/A	0.111	0.047	0.089	0.093	0.086	0.081	0.071	0.056	0.029

θ values ($^{\circ}$)		30.6	78.4	30.5	30.5	42.6	30.5	30.6	33.6	78.4	78.4	30.5
		1.6	7.5	1.9	2.0	0.6	2.0	1.9	2.0	7.5	7.5	2.0
$(\sin\theta/\lambda)_{\max}$ (\AA^{-1})		0.716	–	0.715	0.715	0.951	0.715	0.715	0.779	–	0.625	0.715
Range	h	-11→11	-16→16	-10→11	-11→11	-12→15	-11→10	-11→11	-12→12	-16→16	-10→10	-11→11
	k	-18→18	-25→25	-18→18	-18→18	-24→24	-18→18	-18→18	-19→19	-26→26	-16→16	-18→18
	l	-20→20	-28→28	-20→20	-20→20	-26→21	-20→20	-20→20	-21→22	-28→29	-17→17	-20→20
Refinement												
R(obs)		0.031(0.023/0.029/0.067/0.143)	0.076(0.051/0.13/0.128)	0.033(0.031/0.035/0.093)	0.032(0.026/0.035/0.136)	0.033(0.031/0.034/0.071)	0.032(0.027/0.037/0.112)	0.036(0.031/0.033/0.114)	0.031(0.026/0.029/0.085)	0.066(0.049/0.079/0.152)	0.036(0.029/0.035/0.105)	0.031(0.023/0.062)
R(all)		0.05(0.024/0.034/0.127/0.391)	0.084(0.054/0.121/0.152)	0.070(0.034/0.064/0.323)	0.062(0.028/0.059/0.313)	0.109(0.044/0.108/0.415)	0.062(0.029/0.064/0.322)	0.063(0.033/0.055/0.254)	0.049(0.027/0.044/0.192)	0.072(0.050/0.086/0.179)	0.050(0.030/0.050/0.174)	0.071(0.030/0.173)
GOF (all)		1.34	1.69	1.02	1.19	0.94	1.11	1.66	1.33	1.41	1.46	1.41
GOF (obs)		1.59	1.74	1.45	1.61	1.68	1.54	2.33	1.65	1.42	1.79	1.91
parameters		848	641	640	640	640	640	640	640	620	640	384
constraints		327	202	251	251	251	251	251	251	202	251	151
restraints		0	1	0	0	0	0	0	0	0	0	0
$\Delta\rho_{\max}, \Delta\rho_{\min}$		0.91e \AA^{-3} -0.72e \AA^{-3}	3.73f \AA^{-3} -3.11f \AA^{-3}	0.71e \AA^{-3} -0.54e \AA^{-3}	0.65e \AA^{-3} -0.51e \AA^{-3}	0.92e \AA^{-3} -0.61e \AA^{-3}	0.80e \AA^{-3} -0.50e \AA^{-3}	0.76e \AA^{-3} -0.64e \AA^{-3}	0.82e \AA^{-3} -0.51e \AA^{-3}	3.14f \AA^{-3} -3.07f \AA^{-3}	0.65e \AA^{-3} -0.45e \AA^{-3}	0.55e \AA^{-3} -0.48e \AA^{-3}
<p>^a Number in the parentheses are for main reflections, 1st order satellites, 2nd order satellites and 3rd order satellites (if there are any), respectively.</p> <p>^b Each reflection is treated as an independent reflection from time-of-flight Laue neutron diffraction of sample 7147A because the reflections that have the same or equivalent hkl are almost certainly from different wavelengths, which is a factor in the absorption correction. This also allows the independent refinement of scale factors from different runs.</p>												

3. Structure Refinement

3.1. Neutron diffraction

Single-crystal neutron diffraction follow the same principle (Laue equation) as X-ray diffraction. The main difference is that, instead of the X-ray photons scattered by the electrons in atomic orbitals, the neutrons are scattered by the nuclei in the crystal lattice. Therefore, the scattering factors (or scattering length) of certain element is very different in neutron diffraction than in X-ray diffraction. Neutron diffraction is good for discerning elements that are next to each other (e.g. Al and Si) in the periodic table, because unlike X-ray, the neutron scattering length of nucleus does not scale with atomic number. Another advantage of neutron diffraction is that the cross section of a nucleus is practically a 3D Dirac-delta function, the Fourier transform of which is a constant that does not fall off at high diffraction angles. Therefore, the atom position and anisotropic displacement parameters (ADPs) are much better defined compared to X-ray diffraction, especially when atom sites are close to each other in the case of positional disorder.

The neutron diffraction data collected on TOPAZ are stored as events, with information of the position each individual neutron hits the detector, as well as the time-of-flight (TOF) of the neutron. Neutron TOF Laue technique expands the measured diffraction pattern from 2D on detector spaces to wavelength-resolved 3D volume in (x, y, λ) along the neutron TOF direction. This means the data reduction process for single-crystal neutron diffraction experiment is quite different from X-ray diffraction, and programs written for X-ray data processing cannot be used for reducing neutron diffraction data. *Mantid* (Arnold *et al.*, 2014) program is capable of reducing data from 3D periodic structures, but this represents the first incommensurately modulated (3+1)D structure with triclinic symmetry ever studied with TOF single-crystal neutron diffraction. The only modulated structure ever studied before with neutron TOF single-crystal diffraction before was Rb_2ZnX_4 by Gutmann *et al.* (2008). It had an orthorhombic symmetry which makes it easy to reduce the data with an approximate commensurate supercell. Since there is no commensurate supercell that approximate the incommensurate structure, we have developed new algorithms in *Mantid* to process satellite peaks (Jin, Wang *et al.*, 2019) for the data collected in this work.. Once the diffraction data are reduced to Jana2006-readable format, the structure refinement process is exactly the same as in X-ray diffraction, with only the scattering factors changed to scattering length for the atoms in the structure.

We used the same structural model in the refinement as previously published results (Jin & Xu, 2017*a,b,c*). However, instead of using Ca+Na for the M sites and Al+Si for the T sites, only Ca and Si were used with the occupancies relaxed in the refinement. This is okay in neutron diffraction refinement, because the only difference of scattering powers between different elements is the scale, which can be fully reflected by the occupancy. Whereas in X-ray diffraction, different elements not only have

different numbers of electrons (scattering power), they may also differ in how the electrons are distributed around the nuclei (form factors). The average scattering power of M sites and T sites are constrained by the calculated value from the EPMA analyzed composition. The T site occupancies are eventually converted back to Al and Si occupancies that adds up to unity after the refinement converged for presentation and comparison. Even though we tried our best to avoid twinning when preparing the sample, the crystal used for sample Dul-15-6A still have ~5% of albite twin. This is considered in the refinement process, but seems to introduce some inaccuracy for the exact occupancy of the T sites. Therefore, the discussion around the structures from neutron diffraction would mainly focus on sample 7147A, which has stronger satellite reflections and no twin.

The overall framework structures are no different from the ones refined from X-ray diffraction data, which is expected. The atom positions and ADPs are better defined in the framework. The T site occupancies are directly refined for the first time for *e*-plagioclase structures with modulation, and the results correlate pretty well with the $\langle T - O \rangle$ bond distances. The differences between the refined occupancy and $\langle T - O \rangle$ distances are more likely to be resulting from the uncertainties from the experiment. The difference of scattering length between Al and Si is ~20%, which means a 2% error in T site scattering power from the refinement could convert to a 10% uncertainty in the Al occupancy.

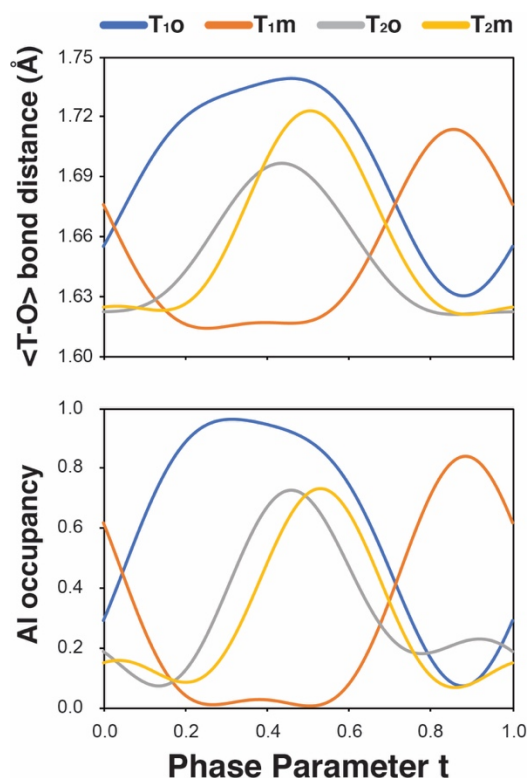


Figure 1 The $\langle T - O \rangle$ distance modulation and T site occupancy modulation from the single-crystal neutron diffraction refinement of sample 7147A ($An_{52.5}$). The exact amplitude for each T site is slightly different but the peak positions (phase of the modulation wave) match perfectly between the $\langle T - O \rangle$ distance and T site occupancy modulation.

The most interesting feature we get from the neutron diffraction is the M site. The nuclear density map from the neutron diffraction data clearly shows three peaks instead of two as shown in X-ray. This feature is independent from the model selected for the refinement, which means the three peaks in the nuclear density map is always there even if only one or two M sites are used in the refinement. To better fit the neutron diffraction data, we added an extra M site to the structure model in the refinement, in between the M_1 and M_2 sites, which we call $M_{1.5}$. The electron and nuclear density maps for the M sites at selected phases (0 , $\frac{1}{4}$, $\frac{1}{2}$, and $\frac{3}{4}$) are presented in Figure 2. The atom positions are much better defined from the neutron diffraction data compared to the X-ray diffraction. Using the 3-split M site model, each individual M site is relatively stationary, with the density map mostly defined by the occupancy distribution between the split sites (Figure 3).

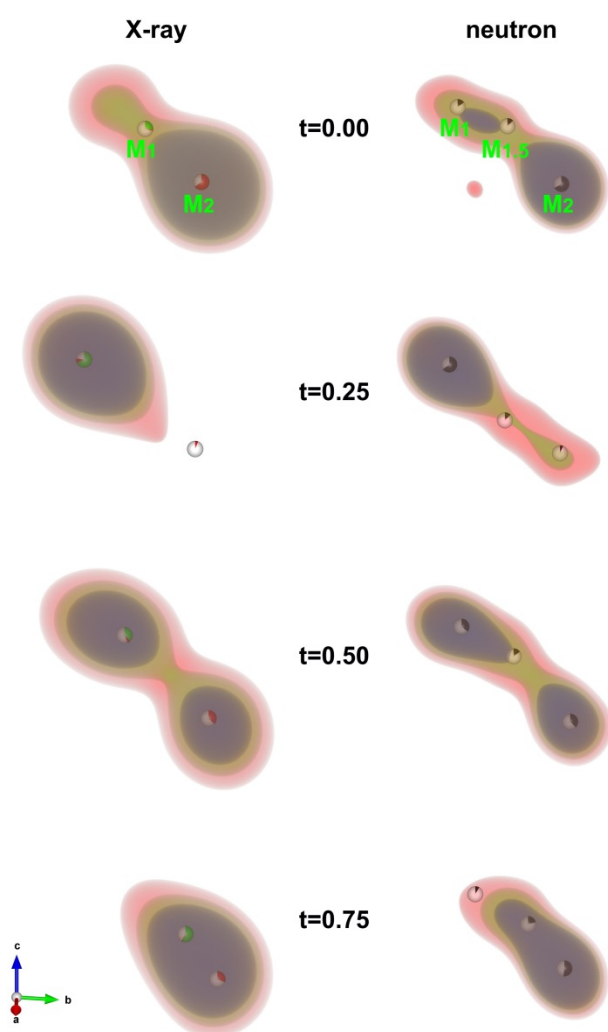


Figure 2 The comparison between electron density map and nuclear density map around the M site in the modulated structure of sample 7147A ($An_{52.5}$) at selected phases (0 , $\frac{1}{4}$, $\frac{1}{2}$, and $\frac{3}{4}$). The nuclear

density map from neutron diffraction refinement clearly shows three maxima at all phases, whereas the electron density map from X-ray diffraction refinement only show two discernible positions.

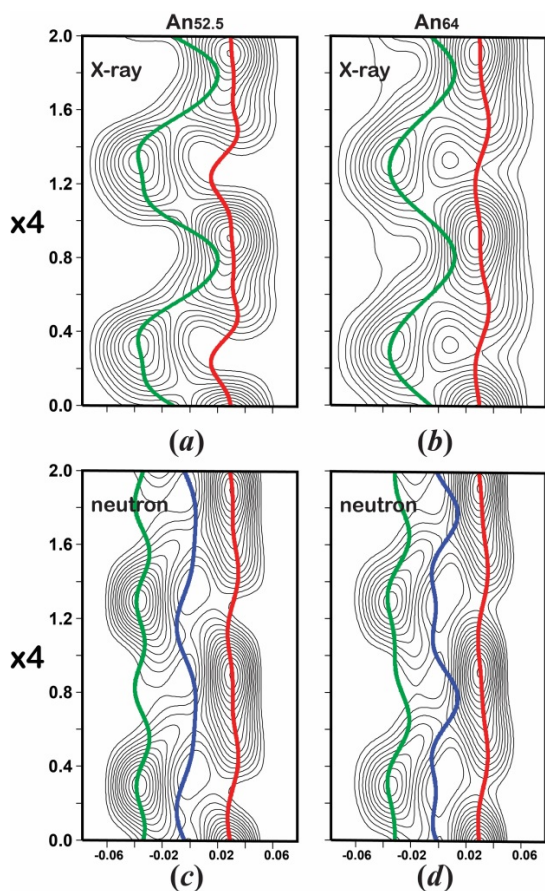


Figure 3 The displacement modulation of the split M sites along the x_2 direction (approximately b -axis) of sample 7147A ($An_{52.5}$) and Dul-15-6A (An_{64}) from both X-ray and neutron diffraction. The contours in the background shows the electron density map (X-ray) and nuclear density map (neutron). Unlike the structure from X-ray diffraction data, the neutron diffraction refined structures with 3-split M site model show that each M site is nearly stationary, with the modulation mainly contributed by the occupancy modulation.

We plotted the occupancy of each individual M site in Figure 4, along with the total occupancy all three split sites. Note that the occupancy here is not the actual atom occupancy of a certain split M site, but reflects the scattering power of the site, contributed by both Ca and Na in that site. Therefore, the total occupancy of all three split sites reflect the modulation of Na component in the M site. We have translated the total occupancy from neutron diffraction refinement to the actual Na occupancy modulation in the structure. We have plotted the Na modulation of all 8 symmetrically equivalent sites within one unit cell in Figure 4 as well, which as pointed by Jin & Xu (2017b), reflects the density modulation of the structure.

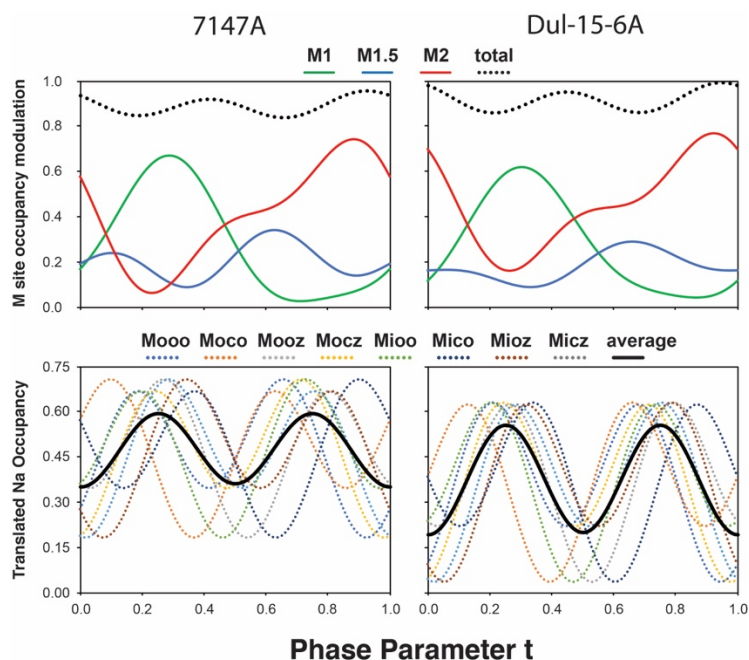


Figure 4 The M site occupancy (scattering power) modulation of an individual M site, along with the modulation of the total scattering power in one M site (top two). The total Na occupancy in each M site can then be calculated from the total scattering power of the M site. The average Na occupancy of all 8 symmetrically equivalent sites in a unit cell shows the density modulation in the structure (bottom two).

Figure 5 shows the relation between the M sites and the surrounding tetrahedra in the modulated structure of sample 7147A. Note that in this figure, the M site is inverted relative to the density maps shown in (Figure 2), otherwise the M site would be obscured by the two tetrahedra behind it. It is impossible to calculate the Ca/Na distribution among three split M sites, even if we combine neutron and X-ray data together. The nuclear density maps at $t=0$ and $t=0.5$, as shown in Figure 2, show obvious three peaks, which are not observed in the neutron diffraction refined $I\bar{1}$ labradorite structures that are recently published. This indicates that the $I\bar{1}$ twin boundaries in the modulated structure of e -plagioclase are not exactly the same as $I\bar{1}$ structures of high-temperature Ca-rich plagioclase.

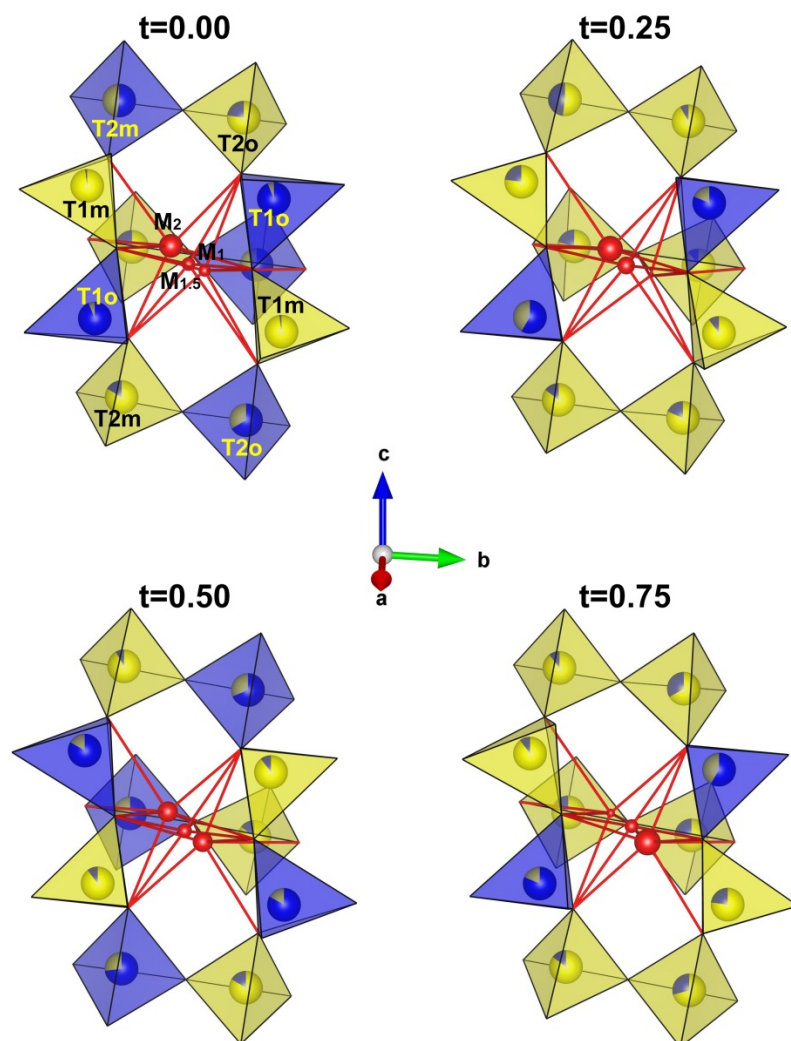


Figure 5 The M site and the surrounding tetrahedra at phase 0, $\frac{1}{4}$, $\frac{1}{2}$, and $\frac{3}{4}$. The occupancy distribution of the M site among three split sites are indicated by the size of the sphere (the projected area of the sphere). The tetrahedra are coloured yellow and blue for Si and Al dominated sites respectively. It is shown that the distribution of the M site occupancy is strongly affected by the relative position of the two tetrahedra beneath them.

Sections of the structure of sample 7147A are shown in Figure 6 for a more complete picture of the modulation in 3D space. The Si and Al dominated tetrahedra are coloured with yellow and blue respectively to enhance the ordering pattern in the framework. The $I\bar{1}$ -like inversion twin boundaries are marked with red planes in the figure. The structure refined from neutron diffraction and X-ray diffraction data are compared side by side. The structure of 7147A is very similar to that of sample 987L (Jin & Xu, 2017b) and sample R2923 (Jin & Xu, 2017c), just with stronger modulation. The Al-Si ordering pattern of the tetrahedral framework is the same between the structure refined from neutron diffraction data and that from X-ray diffraction data, which is already implied by the result shown in

Figure 1. There is no part of the modulated structure that violates the Al-avoidance principle, and the average Al occupancy in the $I1$ -like domain is significantly more the 0.5. The neutron-data-refined structure shows a more detailed M site configuration as discussed in Figure 5. The two M sites that are related by the inversion center in the $I\bar{1}$ -like inversion twin boundaries are concentrated toward the same direction in the $I1$ -like domain.

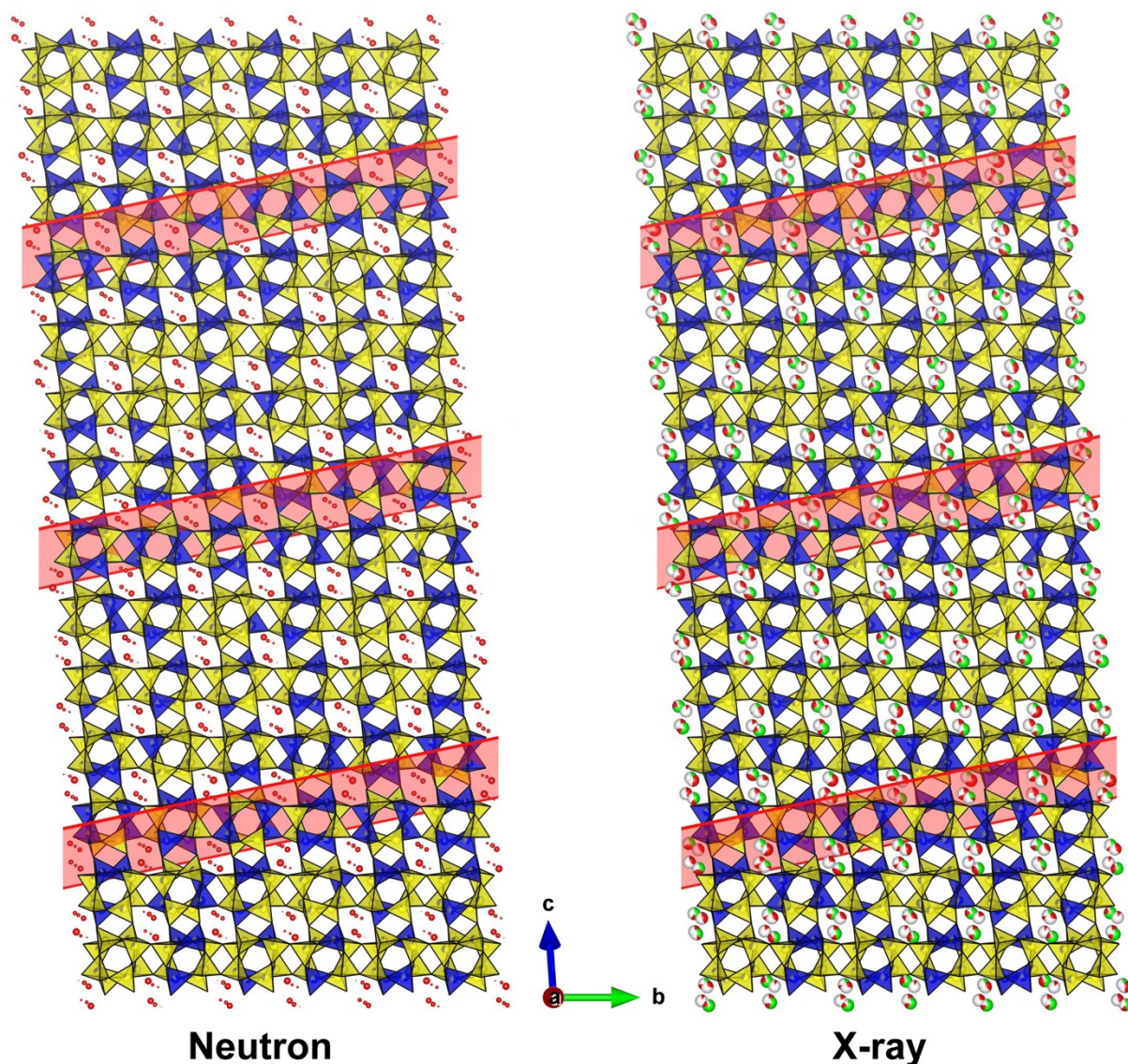


Figure 6 Comparison between the structure of sample 7147A refined from neutron and X-ray diffraction data. Si and Al dominated tetrahedra are coloured in yellow and blue respectively. The Al occupancies in the neutron structure are directly refined from the diffraction data, whereas in the X-ray structure, they are calculated from $\langle T - O \rangle$ bond distances. The configuration of M sites in the neutron structure are illustrated with the relative scattering power of each split site, as in Figure 5. The red planes mark the $I\bar{1}$ -like inversion twin boundaries.

3.2. X-ray diffraction

Unlike recent papers on the $I\bar{1}$ and $e2$ structures of high-temperature plagioclase structures (Jin, Wang *et al.*, 2018; Jin, Xu *et al.*, 2019), there is no ambiguity regarding the symmetry of the structures in this paper. Figure 7 shows $0kl$ precession images of the selected structures studies in this paper. All of the structures in this paper display very sharp and well-defined e -reflections in the diffraction pattern. Even in sample SKHHM(An_{67}) and sample 11044.p3(An_{68}) where the modulation periods are quite long ($\sim 60\text{\AA}$), the e -reflections are obviously separated pairs. The second-order satellite reflections (f -reflections) are observed in all samples except sample 11044.p3 (An_{68}), making it the most calcic $e2$ structure ever reported, followed by the previous record holder, Lake County Sunstone (An_{64}).

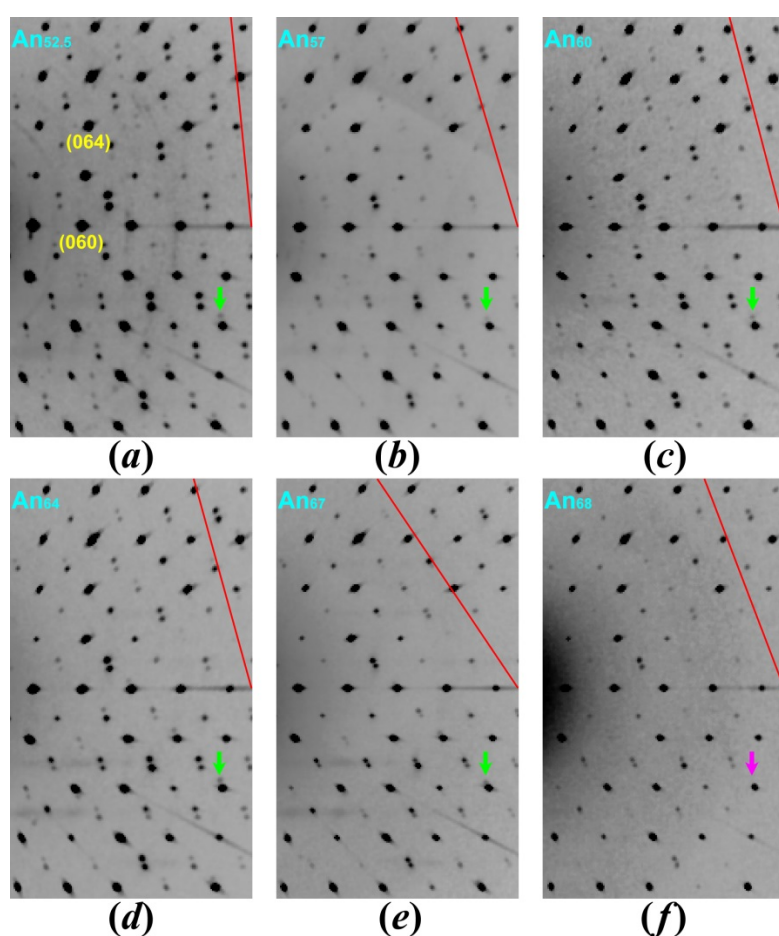


Figure 7 Fractions of the unwarped $0kl$ precession images of selected samples from this work. (a) 7147A($An_{52.5}$); (b) 89GM97(An_{57}); (c) 67796b(An_{60}); (d) Dul-15-6A(An_{64}); (e) SKHHM(An_{67}); (f) 11044.p3(An_{68}). The red lines mark the modulation orientation projected on $0kl$ plane. The green arrows mark f -reflections which is absent in sample 11044.p3(An_{68}).

The structure models for both $e1$ and $e2$ structures have been described and discussed in detail in recent papers, and the same models are used in this paper. A significant amount (691) of third-order satellite peaks are observed in the diffraction pattern of sample 7147A, therefore, 3 modulation waves are used for each modulation function in the refinement. This is not the first time third-order satellite peaks are observed in e -plagioclase. However, the other two reports of third-order satellite peaks are also found in iridescent labradorite samples with exsolution lamellae (Boysen & Kek, 2015; Jin & Xu, 2017c). The importance of f -reflections and their relation to the density modulation has been discussed thoroughly by Jin & Xu (2017b), therefore, the third or even higher modulation waves will not change the structure in any fundamental level. The modulation functions will be better defined with third-order satellite peaks. The result does not seem to affect the comparisons in this paper.

The same 2-split model as previously published structures (Jin & Xu, 2017a,b,c) is used for the X-ray data refinement, with M_2 only occupied by Ca and M_1 containing both Ca and Na. The detailed configuration of M site we obtained from the neutron diffraction data will not improve the X-ray data refinement, simply because the split sites are too close together so their orbital electrons are seriously overlapped with one another. This, however, does not compromise the credibility of the structure refinement from X-ray diffraction data. As pointed out by Jin & Xu (2017b), it is the total scattering power of the M site, which reflects on the Na occupancy modulation, that we should take from X-ray diffraction data. And the difference in scattering power between Ca and Na is more significant in X-ray diffraction than neutron diffraction, the result about density modulation from X-ray data should be more reliable. The Al occupancies of tetrahedral sites are calculated by the $\langle T - O \rangle$ bond distances, following the same equations (Kroll & Ribbe, 1983):

$$Occ(Al)_i = 0.25(1 + n_{An}) + (\langle T_i - O \rangle - \langle T - O \rangle)/k$$

, where the value of k is estimated to be 0.135 as usual (Angel *et al.*, 1990; Jin & Xu, 2017a,b,c).

The $\langle T - O \rangle$ bond distances modulation of the nine structures refined in this paper are plotted in Figure 8. The amplitude of the $\langle T - O \rangle$ bond distances modulations are very similar among the structures. Even the $e2$ structure of sample 11044.p3 shows $\sim 0.1\text{\AA}$, while the satellite peak intensity is obviously much weaker compared to the $e1$ structures in Figure 7. The shape of the modulation curves, on the other hand, can be quite different from one to another. The $\langle T - O \rangle$ bond distances of sample 7147A($An_{52.5}$) shows a section of constant $\langle T_1o - O \rangle$ and $\langle T_2m - O \rangle$ distances between phase parameter $t=0.25$ and $t=0.5$. Similar features can be found in sample Volga Blue (both yellow and colorless), but not in sample 89GM97 or SKHHM. A potential way to quantify this difference in the shape of the modulation function is by the $\langle T_1o - O \rangle - \langle T_1m - O \rangle$ difference at $t=0.2$ (marked by red line in Figure 8).

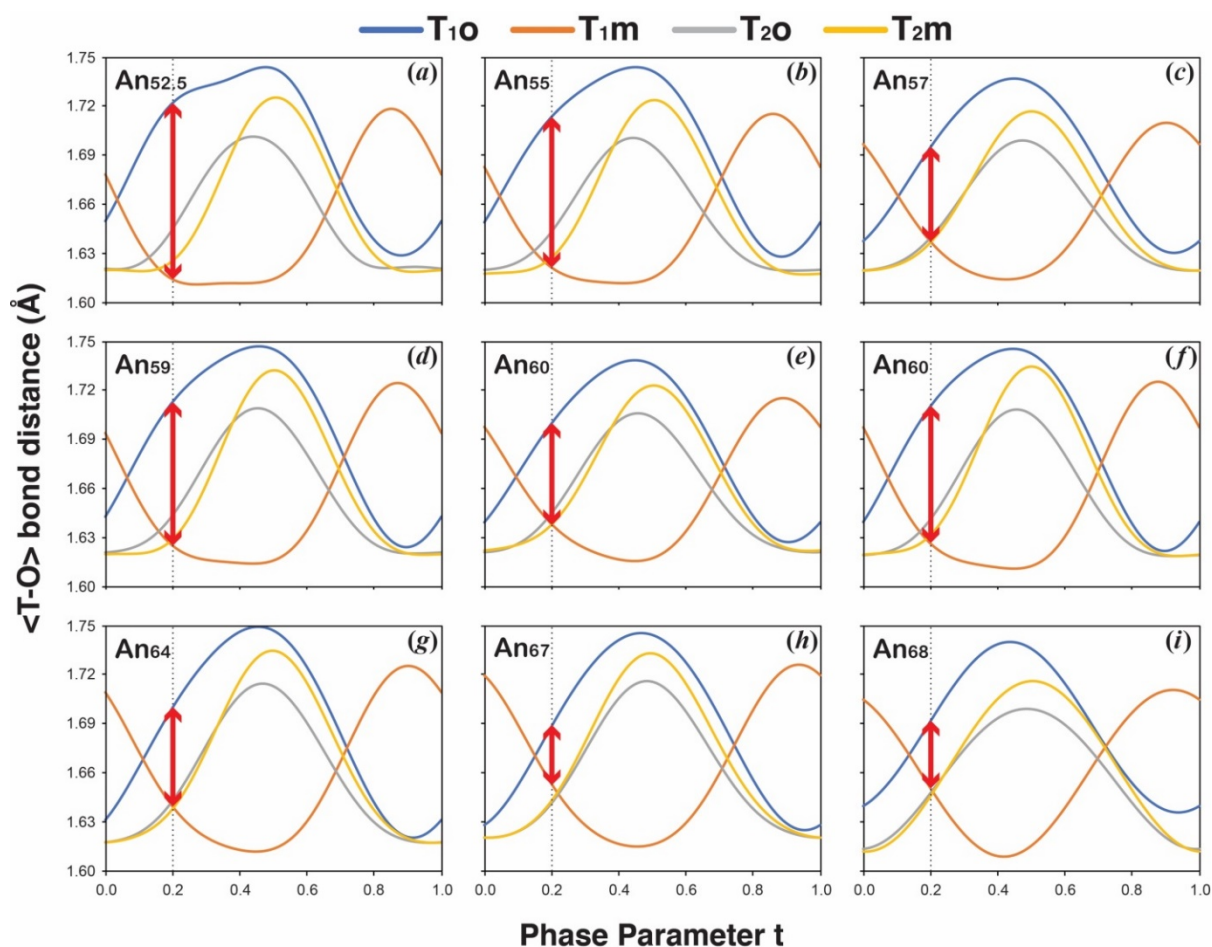


Figure 8 $\langle T - O \rangle$ bond distance modulations of the samples studied in this work. (a) 7147A ($An_{52.5}$); (b) Volga Blue-yellow (An_{55}); (c) 89GM97 (An_{57}); (d) Volga Blue-colorless (An_{59}); (e) 11044.p3 (An_{60}); (f) 67796b (An_{60}); (g) Dul-15-6A (An_{64}); (h) SKHHM (An_{67}); (i) 11044.p3 (An_{68}). All the samples show similar amplitude of modulation, even though degrees of ordering vary a lot from sample to sample. The red segments mark the difference between $\langle T_{1o} - O \rangle$ and $\langle T_{1m} - O \rangle$ at $t=0.2$, which show great variation between different samples, which might be used for quantifying the ordering states of e -plagioclase structures.

Another known way to quantify the degree of ordering in the incommensurately modulated structures of e -plagioclase is by the amplitude of density modulation. The density modulation is the chemical variation in e -plagioclase along the modulation direction. It only exists in $e1$ structures where f -reflections are observed. The $I1$ -like domains of the modulated structure are less calcic compared to the $I\bar{1}$ -like inversion twin boundaries. The $e2$ structure, on the other hand, is chemically homogeneous throughout the crystal, with only displacement modulation and local ordering of Ca/Na and Si/Al within each unit cell. To reveal the density modulation in the structure, we have to average the Na (or Ca) occupancies of all 8 symmetrically equivalent sites within each unit cell ($\sim 8\text{\AA} \times 13\text{\AA} \times 14\text{\AA}$ as in Table

2). The Na occupancy modulations of all nine samples are plotted in Figure 9. Except for the $e2$ structure of sample 11044.p3, all the samples show at least 10% variation of Na occupancy (or mole% An in the composition) in the modulation. Sample 67796b(An_{60}) shows the strongest density modulation, with a compositional difference of ~ 25 mole% An between the inversion twin boundaries and $I1$ -like domains. It is closely followed by sample 7147A($An_{52.5}$) with a $\sim 22\%$ density modulation. Sample SKHHM and sample Dul-15-6A shows density modulation around 18%. The other four samples, Volga Blue (both yellow and colorless), sample 89GM97 and 11044.p1, all show density modulations around 11%.

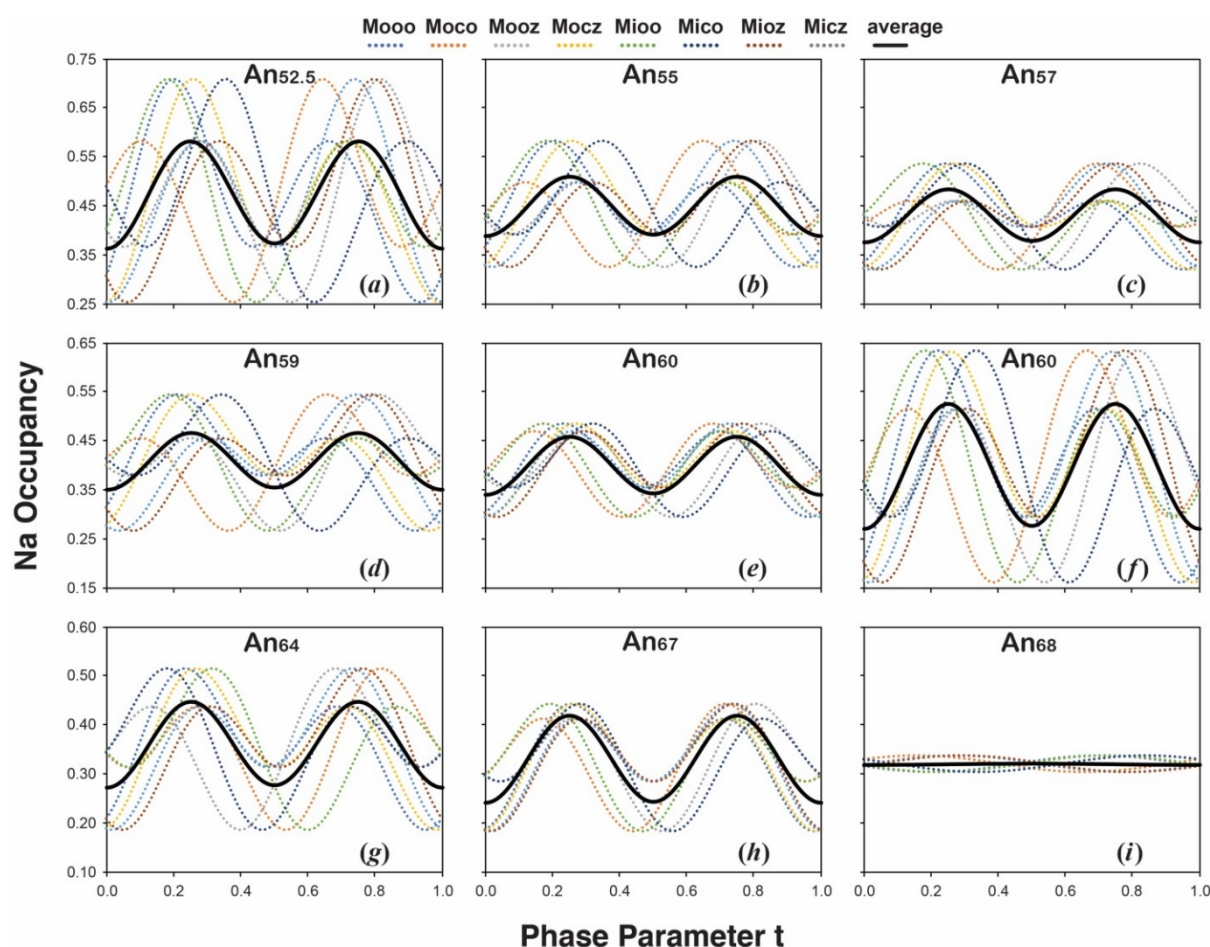


Figure 9 Na occupancy modulation of 8 symmetrically equivalent sites within one anorthite cell of the samples studied in this work. (a) 7147A ($An_{52.5}$); (b) Volga Blue-yellow (An_{55}); (c) 89GM97 (An_{57}); (d) Volga Blue-colorless (An_{59}); (e) 11044.p3 (An_{60}); (f) 67796b (An_{60}); (g) Dul-15-6A (An_{64}); (h) SKHHM (An_{67}); (i) 11044.p3 (An_{68}). All samples show density modulation except sample 11044.p3 (An_{68}).

It is worth pointing out that the density modulation refined from neutron diffraction appears to be stronger than that from X-ray diffraction, especially for sample Dul-15-6A. However, in X-ray

diffraction, the scattering power of Ca is more than 80% stronger than Na, which makes the result regarding the total Na occupancy of M site from X-ray diffraction much more reliable compared to the neutron diffraction data, where the difference is only $\sim 30\%$. It is also interesting that the amplitude of density modulation is not always proportional to the variation of individual Na occupancy modulation. For instance, the variation of individual Na occupancy modulation function of sample 7147A ($An_{52.5}$) is $\sim 45\%$ almost double to the 26% from sample SKHHM (An_{67}), but the density modulations of the two are very similar (22% vs 18%).

4. Discussion

We have covered almost the entire compositional range of *e*-plagioclase ($\sim An_{25}$ – $\sim An_{75}$) so far, therefore, it is time to take a more comprehensive picture of the puzzling incommensurately modulated structures. For the convenience of this discussion, a binary diagram of plagioclase solid solution series is provided in Figure 10, along with the metastable phase diagram proposed by Jin, Xu *et al.* (2019). The diagram is a composition of the results from several most recent papers. It is still not 100% complete, with the complexity mainly focused on the connection between the Bøggild intergrowth gap and the Huttenlocher intergrowth gap, but it will not affect the point of this paper.

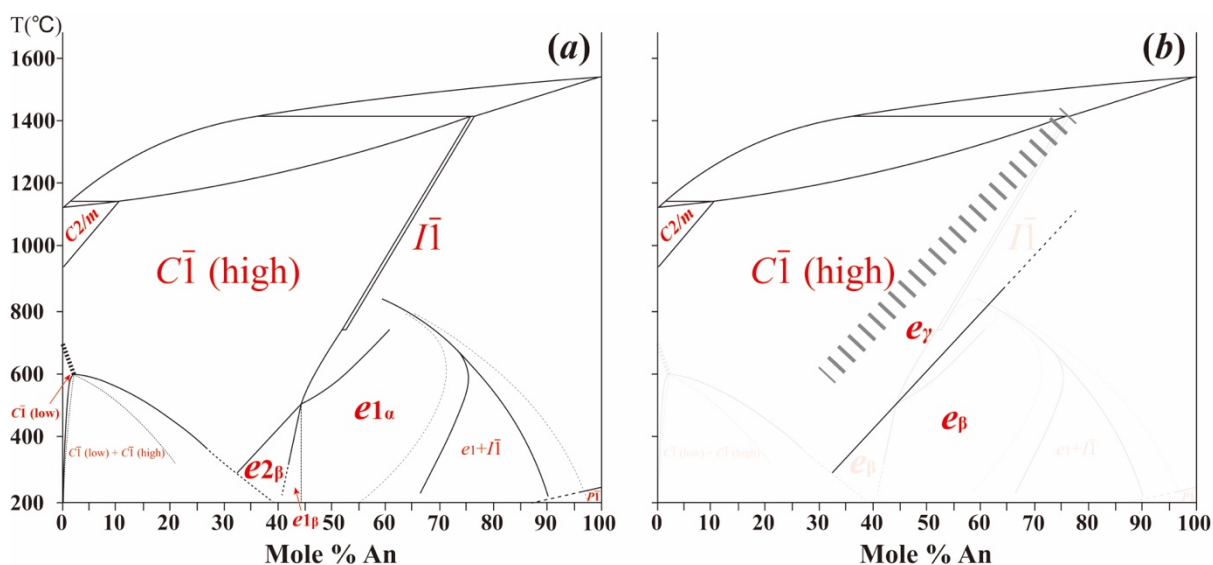


Figure 10 (a) Binary phase diagram of the solid solution series between albite and anorthite, the dash line around Huttenlocher gap is the speculated strain free boundary between $I\bar{1}$ and $e1$; (b) the metastable phase diagram showing the relation between $C\bar{1}$ and *e*-plagioclase as proposed by Jin, Xu *et al.* (2019), a transition zone e_γ is added in the diagram representing the structure with weak and diffuse *e*-reflections.

It has been clear that the difference between $e1$ and $e2$ structure is that $e1$ shows density modulation characterized by the appearance f -reflections, and $e2$ has no f -reflection and no density modulation (Jin & Xu, 2017*b,c*). It has also been reported that some plagioclase would turn from $C\bar{1}$ to $e2$ structure first, and later develop density modulation ($e1$) as the temperature drops further (Jin & Xu, 2017*c*). This type of $e1$ structure is characterized by the distinctively longer modulation period with respect to the mole% An composition (Jin & Xu, 2017*a,c*). We have plotted the three components of the q -vector (irrational indices δh , δk and δl along a^* -, b^* - and c^* -axis), as well as the modulation period, against the compositions of the e -plagioclase (in mole% An) in Figure 11. As pointed out by Jin & Xu (2017*a*), the data points form a band of constant width, most obvious for δh and δl . And all the e -plagioclase samples from igneous rocks (orange data points in the figure) falls on either end of the band (turquoise and green dotted line), supporting the observation made by Jin & Xu (2017*a*). The plot of δk is not as linear as those of δh and δl . It starts to plateau after An₅₅ at around 0.06, which have not been observed before, since no $e1$ structure more calcic than An₅₅ have been studied with accurate q -vector measurement.

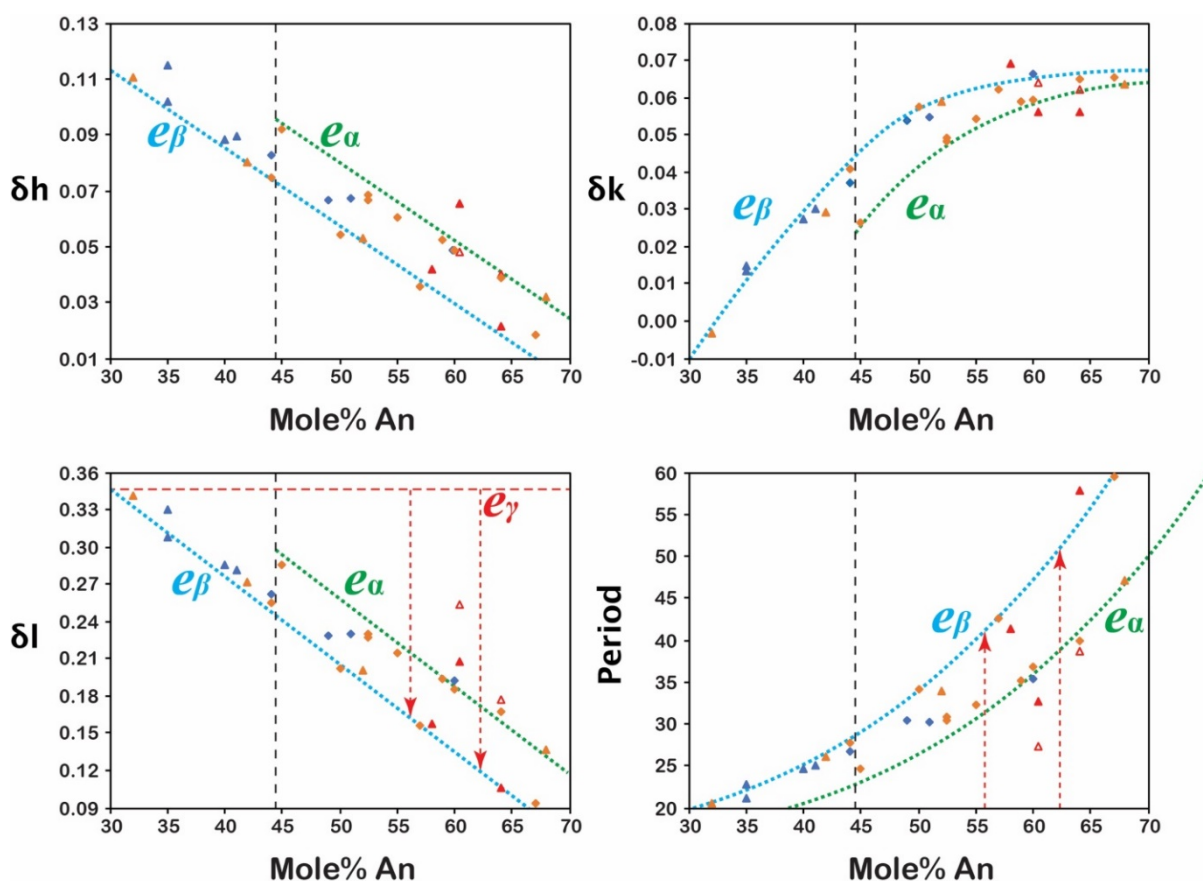


Figure 11 The three components of q -vectors (irrational indices δh , δk and δl along a^* -, b^* - and c^* -axis) along with the modulation period plotted against the composition (in mole% An). The δh and δk plotted against δl is provided in Figure S1.

The two trends of q -vectors followed by the e -plagioclase structures with different compositions had been called “ $e1$ trend” (green dotted line) and “ $e2$ trend” (turquoise dotted line). This, however, is not very convenient for discussion, and may sometimes be confusing, like when we talk about $e1$ structure that follows the “ $e2$ trend”. This is especially a problem in this paper, since we find the structure of 11044.p3, a $e2$ structure, shows a q -vector that lies on the line with shorter modulation period, which is considered a feature of $e1$ structure. The two critical features of e -plagioclase, density modulation and q -vector, are strongly related to each other, but not the same. Therefore, we think it is better to denote the structural difference in q -vector with a different name, e_α and e_β . For a given composition, the structure with relatively shorter modulation period would be e_α and those with longer modulation period would be e_β . This way, we can describe the two features separately in the discussion. A $e1$ structure that has a shorter modulation period (lies on the green line in Figure 11), would be $e1_\alpha$; a $e1$ structure with a longer modulation period would be $e1_\beta$; a $e2$ structure with longer modulation period is $e2_\beta$; and finally, a $e2$ structure with shorter modulation period $e2_\alpha$.

Most of the samples studied in this work show e_α structures, which is expected considering they are all relatively well-ordered from plutonic and metamorphic rocks. The e_α structure appear only when all traces of the $C\bar{1}$ high-albite structure got reset by going through an intermediate stage. Forming exsolution lamellae in the Bøggild intergrowth gap is one way to reset the $C\bar{1}$ structure, and forming the $I\bar{1}$ anorthite structure before forming e -structure is another. For composition between $\sim An_{45}$ and $\sim An_{55}$, $I\bar{1}$ structure is not stable at any temperature, therefore, going through the first-order transition from $C\bar{1}$ to $e1$ is the only way to develop e_α structure. This only happens in extremely slow cooled plutonic plagioclase, such as sample H4-04 (An_{45}) (Jin & Xu, 2017a), R2923 ($An_{52.5}$) (Jin & Xu, 2017c), 7147A ($An_{52.5}$) and Volga Blue-yellow (An_{55}).

For e -plagioclase more calcic than $\sim An_{58}$, the e_α structure are more easily accessible compared to the more sodic compositions. Sample 11044.p1 (An_{60}) from a gabbro in the Duluth igneous complex, shows a e_α q -vector in the modulated structure, which indicates it must have gone through the $I\bar{1}$ structure before turning into e -plagioclase ($e1$). This should be considered an evidence that $I\bar{1}$ structure is a thermodynamically stable phase for this composition (An_{60}) between the $C\bar{1}$ and $e1$ phases, in agreement with the lab experiment by Carpenter (1986). Even though the $I\bar{1}$ structure is kinetically less favorable than the $e2$ structure, it is not nearly as hard to form compared to the exsolution lamellae in the Bøggild intergrowth gap. If the plagioclase stayed in between $C\bar{1}/I\bar{1}$ boundary (double solid line) and the $C\bar{1}/e2$ boundary (extended dash line) for a sufficiently long time, it will most certainly turn to $I\bar{1}$ structure, since that is the thermodynamically stable structure.

Of the samples studied in this work, only sample 89GM97 and sample SKHHM are e_β . As previously mentioned, e_β appears as a result of the second-order phase transition from $C\bar{1}$ to $e2$. This means all plagioclases with a composition less calcic than $\sim An_{44}$ are e_β , because there is no other path to e -

plagioclase in this compositional range (Jin & Xu, 2017a). Things are more interesting with higher calcic composition, where the e_β could happen as a result of the metastable phase transition from $C\bar{1}$ to $e2$, as it is kinetically favorable compared to the other options (Jin & Xu, 2017c). Sample 89GM97 (An₅₇) should have similar cooling rate as sample 11044.p1 (An₆₀). It formed e_β structure because it falls in the composition range of Bøggild intergrowth gap, where the $I\bar{1}$ structure is not a stable phase (or the stable area for $I\bar{1}$ is too small to be effective). Sample Dul-15-8A (An₅₂) and sample SK90-12 (An₅₀) (Jin & Xu, 2017c) followed similar process as sample 89GM97, just less ordered with faster cooling rate.

It is a bit surprising that sample SKHHM shows a e_β structure even with a composition as calcic as An₆₇. The stable area of the $I\bar{1}$ structure is much larger at this composition, and the sample should have stayed between $\sim 1100^\circ\text{C}$ and $\sim 900^\circ\text{C}$ for at least hundreds of years (Grove, 1982; Grove *et al.*, 1984; Ganguly & Domeneghetti, 1996; Holness *et al.*, 2007). This means the transition from $C\bar{1}$ to $I\bar{1}$ is really hard under dry conditions. It is also possible that the metastable transition from $C\bar{1}$ to $e2$ initiates at higher temperature than the linear extension indicated in the Figure 10b, since we have not seen any real $C\bar{1}$ structure with no diffuse scattering around the e -positions. This means all the $I\bar{1}$ structures are actually converted from poorly developed $e2$ structure, which makes it much harder kinetically. We have also measured the q -vectors of sample 54091 from Bushveld (Carpenter & McConnell, 1984; Carpenter, 1986) to be $q=0.01102a^*+0.07033b^*-0.07859c^*$, with a modulation period of $\sim 66\text{\AA}$. This is the longest modulation period found in any e -plagioclase, which indicates a e_β structure at the composition of $\sim\text{An}_{75}$. [The previously reported $\sim 80\text{\AA}$ period by McLaren (1974) is from electron diffraction, which measured a 2D projection of the 3D q -vector. And calculating the projection of our q -vector onto the same zone axis gives similar result.] This means the e_β structure can happen with even more calcic compositions. The structure of sample 54091 is not refined in this work, because it is not a pure phase (Huttenlocher intergrowth between $I\bar{1}$ and $e1$), and the satellite peaks are too close together to be integrated reliably.

The e -reflections in the volcanic phenocrysts are normally weak and diffuse, therefore the q -vectors are relatively poorly defined. And the q -vectors also depends on the ordering states of the structure as discovered by Jin, Xu *et al.* (2019). We suggest to call these volcanic phenocryst e -plagioclases with diffuse and “moving” satellite peaks e_γ , to separate them from the e_α and e_β structures where the q -vectors do not change with ordering states. Jin, Xu *et al.* (2019) speculated that all disordered $C\bar{1}$ structure start showing e -reflections around the same positions in reciprocal space, independent from the composition, which are governed by the Anti-Rigid Unit Modes (ARUM) of the tetrahedral framework. The q -vector moves towards the e_β line as the modulation gets stronger in the structure. The satellite peaks would stop moving once they reach the e_β line (Jin, Xu *et al.*, 2019). This process happens pretty fast, as Lake County Sunstone sample already reached the e_β line (Jin, Xu *et al.*, 2019). Therefore, it is safe to say that the e_γ structures are only preserved in quenched volcanic plagioclases.

We also plotted the orientation of the q -vectors of the e -plagioclase structures on to a stereograph projection in Figure 12. As pointed out by Smith & Brown (1988), all data points fall nicely in the $[923]$ zone axis (except some volcanic samples with diffuse and poorly defined satellite peaks). This could explain why the δk plot in Figure 11 is not linear. It is not clear what is the significance about zone-axis $[923]$ in the plagioclase structures and the modulations. Unlike the stereonet projection by Smith & Brown (1988), where the calcic e -plagioclase would have q -vector that has greater to 90° angle with $[100]$ zone-axis (right side of the blue vertical line in Figure 12), the q -vector of the most calcic e_β structure would get near $(01\bar{1})$, but never cross the $[100]$ zone axis trace. It appears $\sim\text{An}_{75}$ would be the limit for the most calcic e -plagioclase in nature, because slowly cooled e_α structure would enter the Huttenlocher intergrowth gap and exsolve into e -plagioclase with less calcic compositions, and e_β structure would require $C\bar{1}$ structure at crystallization, which is not stable for compositions more calcic than $\sim\text{An}_{75}$.

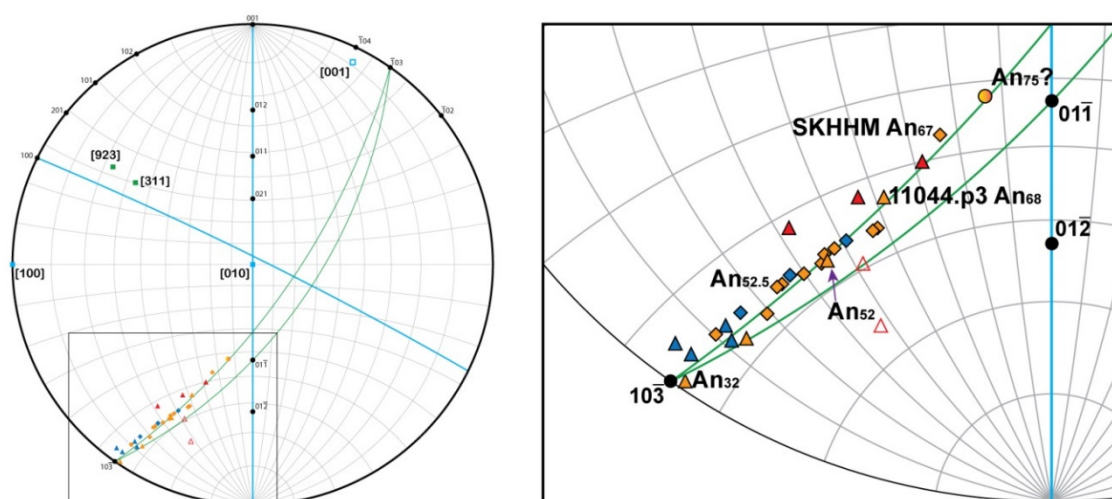


Figure 12 Stereonet projection of the q -vectors of the samples studied in this paper and some recently published papers. The q -vectors all lie almost exactly on the $[923]$ zone axis, tilting away from $(10\bar{3})$ with increasing An number in the composition. The q -vectors plotted covers the entire compositional range of e -plagioclase (e -reflections in samples more sodic than An_{30} are too weak and diffuse to be measured).

Sample 11044.p3(An_{68}) is the only e_2 structure refined in this work, no f -reflections (second order satellites) were detected, therefore no density modulation in the structure (Figure 9). This is also the first $e_{2\alpha}$ structure ever observed. With similar cooling rate as sample 11044.p1(An_{60}), it is expected that sample 11044.p3(An_{68}) would transform to the $I\bar{1}$ structure first before entering the e_1 area. The e_2

structure of sample 11044.p3(An_{68}) shows that not all e -plagioclase that transformed from the $I\bar{1}$ structure has to be $e1$. This could mean that all $e1$ structures from igneous rocks, no matter $e1_\alpha$ or $e1_\beta$, must have all went through the $e2$ stage with no density modulation.

The fact that 11044.p3(An_{68}) less ordered than 11044.p1(An_{60}) suggests the negative slope of the $I\bar{1}/e1$ boundary, where the transition temperature drops with increasing Ca concentration in the composition, since both structures should have similar cooling rate, and they all went through the same path ($C\bar{1} \rightarrow I\bar{1} \rightarrow e_\alpha$). Another evidence for this is from sample Dul-15-6A (An_{64}), which is an anorthosite xenolith in the Duluth Igneous Complex. It is considered to have similar origin as sample 28-88 (An_{66}) (Jin, Wang *et al.*, 2018), which is from an anorthosite xenolith in the Beaver Bay Complex. Sample 28-88 (An_{66}) has an $I\bar{1}$ structure but sample Dul-15-6A (An_{64}) shows $e1$ structure with strong density modulation, suggesting the e -plagioclase structure is easier to form with less calcic composition (between $\sim An_{60}$ and $\sim An_{70}$).

Based on the symmetry relations between $I\bar{1}$ and e -plagioclase ($X\bar{1}$), the phase transition between the $I\bar{1}$ and $e1$ must be first-order, because the superspace group $X\bar{1}(\alpha\beta\gamma)0$ is not a subgroup of space group $I\bar{1}$. However, unlike the first-order boundary between $C\bar{1}$ and $e1$, which results in the Bøggild miscibility gap, there is no evidence of exsolution lamellae for plagioclase with composition between $\sim An_{60}$ and $\sim An_{70}$. This must be because the gap between $I\bar{1}$ and $e1$ is very narrow, so there is not enough energy advantage for phase separation to overcome the excessive boundary energy. [The intergrowth between An_{61} and An_{69} found in metamorphic rock (Phillips *et al.*, 1977) could be caused by the boundary between $I\bar{1}$ and e -plagioclase, but it is impossible to be certain without more evidences.] More importantly, the Huttenlocher intergrowth ($\sim An_{66}$ and $\sim An_{90}$) is between $I\bar{1}$ and $e1$, which is also a first-order phase boundary between the two structures. Now that we know the e -plagioclase structure is actually a thermodynamically stable phase, the Huttenlocher miscibility gap is no other than the extension of the $I\bar{1}/e1$ boundary at more calcic composition. Therefore, if the $I\bar{1}/e1$ has a negative slope between $\sim An_{60}$ and $\sim An_{70}$, the Huttenlocher gap must be at lower temperature compared to the Bøggild miscibility gap, unlike in previously proposed phase diagrams, where Huttenlocher gap occurs at either much higher temperature (Nord Jr *et al.*, 1974; McConnell, 1974; Smith, 1984) or at the same peak temperature (Carpenter, 1994). We used solid line in Figure 10a to mark the $I\bar{1}/e1$ boundary which expands into the Huttenlocher gap at lower temperature, and dash lines to outline possible strain-free boundaries for this miscibility gap.

The diffuse c -reflections in the diffraction patterns of volcanic phenocrysts were explained with the disordered tetrahedral frame work by Jin, Wang *et al.* (2018). We still have to address the weak and diffuse c -reflections in the well-ordered e -plagioclase. The h $h-2$ l precession images of selected samples are presented in Figure 13, along with heated volcanic phenocryst MXCG from Jin, Xu *et al.* (2019). The c -reflections of all the samples studied in this work are not as strong as in the heated MXCG (An_{58})

sample (Figure 13*f*), which supports the theory that the c -reflections are not from the e -plagioclase structure, and they are more prominent in disordered structures. However, the c -reflections in sample Dul-15-6A (An₆₄) (Figure 13*d*) and sample SKHHM (An₆₇) (Figure 13*e*) are quite obvious and needs some explanations. It seems the intensities of the c -reflections generally increase with increasing anorthite concentration in the composition. It is possible that the c -reflections are from the $I\bar{1}$ -like inversion twin boundaries in the e -plagioclase structure, therefore their intensities depend both on the bulk composition of the crystal and the amplitude of the density modulation. The local composition of the $I\bar{1}$ -like inversion twin boundaries in sample Dul-15-6A (An₆₄) and sample SKHHM (An₆₇) are \sim An₇₃ and \sim An₇₆ respectively, it should not be a surprise if they would collapse into $P\bar{1}$ -like domains at the temperature of data collection (100K), where only the end member albite and anorthite structures should be stable. It is also possible that the path through $I\bar{1}$ -stable area may also affect the intensities of c -reflections.

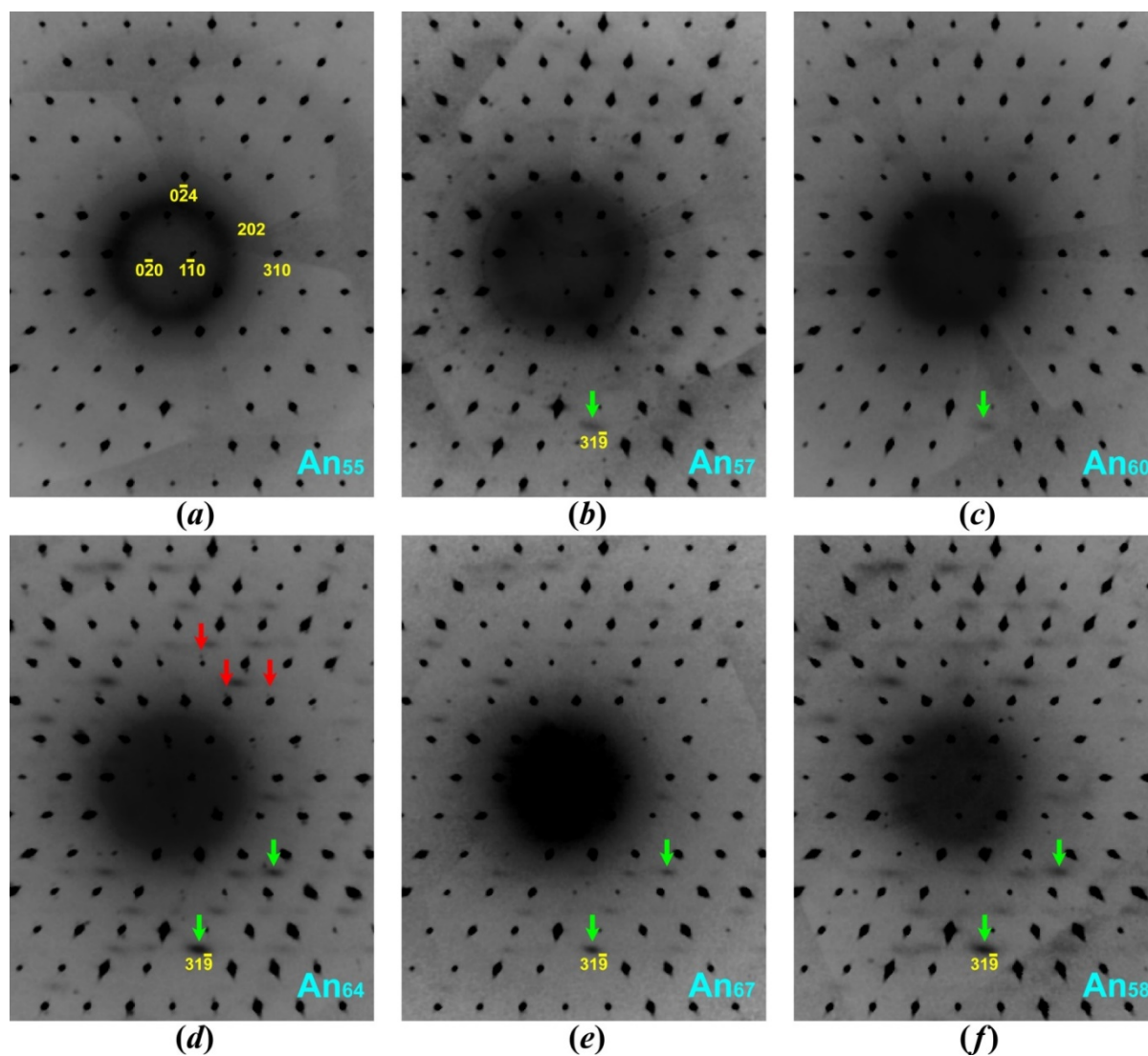


Figure 13 The $h h-2 l$ precession images of selected samples to compare the c -reflections in the diffraction pattern. (a) Volga Blue-yellow (An₅₅); (b) 89GM97 (An₅₇); (c) 11044.p3 (An₆₀); (d) Dul-15-6A (An₆₄); (e) SKHHM (An₆₇); (f) MXCG (An₅₈) for comparison (Jin, Xu *et al.*, 2019).

5. Implications

Of the lattice parameters of the plagioclase structure, the interaxial angle γ (angle between a - and b -axis) is the most sensitive to the ordering state of the structure. Jin & Xu (2017a) realized that the kinks in the γ angle trend of the most ordered plagioclase can be explained by one jump around An₄₄ due to the termination of Bøggild miscibility gap (Figure 10). We make the same γ angle plot against mole% An composition in Figure 14, with composition range expanded to An₇₅. It shows that even with the new data included, the data still fits the trends proposed by (Jin & Xu, 2017a) quite well. The e_1 and e_2 structures can be nicely separated by a straight line with only a couple of exceptions (sample 89GM69 at An₄₁ and sample 11044.p3 at An₆₈). It is interesting that the γ angles are more sensitive to the ordering states of disordered volcanic sample (red triangles in Figure 14), but does not change much for the well-ordered e_1 structures. For example, it is almost impossible to compare the ordering states of the e_1 structures of sample 89GM97(An₅₇), sample 11044.p1(An₆₀), sample Dul-15-6A(An₆₄) and sample SKHHM(An₆₇) only based on the γ angle. The $\langle T_1O - O \rangle$ distances plotted against composition shows very similar pattern as the γ angle plot, which can be found in Figure S2.

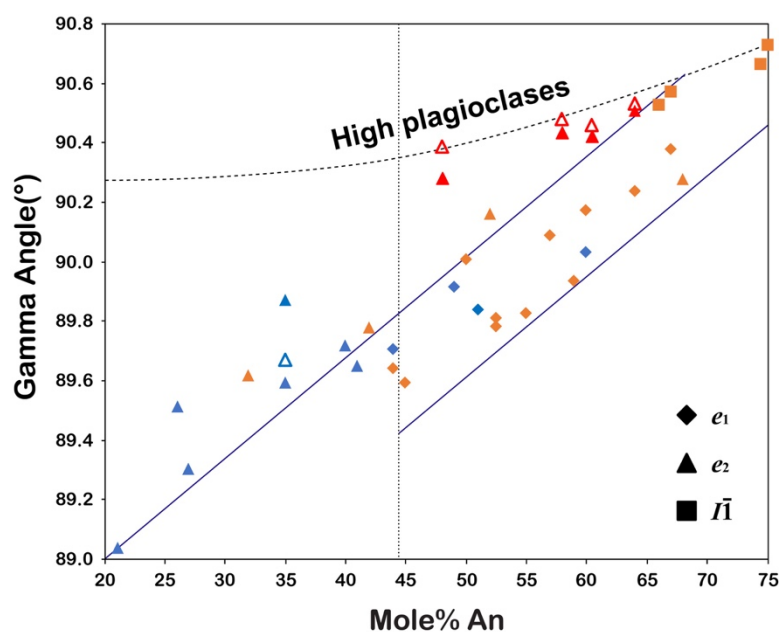


Figure 14 Interaxial γ angles (between a - and b -axis) plotted against composition (in mole% An). Data from samples in this paper and several recently published papers (Jin & Xu, 2017a,b,c; Jin, Wang *et al.*, 2018; Jin, Xu *et al.*, 2019). The lines roughly outline the zones for e_1 and e_2 structures.

As shown in Figure 8 and Figure 9, comparing the ordering states of *e*-plagioclase structures with different compositions is very difficult. It is hard to find one universal factor from the structure that can be used for quantifying the ordering state. This is mainly due to the complicated subsolidus phase relations of the solid solution series, which results in several different paths that may lead to the *e*-plagioclase structure. One way to bypass this issue is to go back to the raw data or the integrated peak intensities. We plotted the normalized intensities of peak $(071\bar{1})$ (most intense peak in $0kl$ plane) against the mole% An composition in Figure 15. The data from samples studied in this work are labeled by their names or numbers. Individual reflection might be subject to errors in the experiment and reduction process, but normalizing *e*-reflections to their adjacent *a*-reflections should help eliminate the systematic errors from the data collection process. One big advantage of this method for estimating the ordering state of *e*-plagioclase is the simplicity. There is no need for a full data collection, one frame of diffraction is all you need once the orientation of the mounted crystal is measured.

intensity, sample 67796b (An₆₀) shows much stronger density modulation than Volga Blue-colorless (An₅₉) (Figure 9). Sample 67796b is an anorthositic granulite, which is an orthometamorphic rock with igneous origin, which means it had the chance to enhance the density modulation during the metamorphism in addition to the original cooling after crystallization. It is also worth noting that sample 11044.p3(An₆₈) shows stronger (071 $\bar{1}$) peak than sample SKHHM (An₆₇), even though it is a *e*2 structure with no density modulation. Moreover, the transition temperature between $C\bar{1}$ and *e*2 is too low for plagioclase less calcic than An₄₅ and the ordering is mainly driven by the Al ordering in T₁₀ site within the $C\bar{1}$ space group. Therefore, the intensities of the *e*-reflections are generally much lower, and not as sensitive to the ordering state or cooling rate of the sodic plagioclase.

The incommensurately modulated structures and exsolution textures of intermediate plagioclase can record processes that cover a wide range of time scales: from changes happening within weeks in the volcanic phenocrysts to the Bøggild intergrowth that takes billions of years to form. This shows great potential for a universal cooling rate speedometer. However, the subsolidus phase relations of plagioclase solid solution series have multiple layers to it, and the incommensurately modulated structure of *e*-plagioclase also has many aspects and require several parameters to fully describe. The complexity of the system indicates the potential to take more information from it, but it also increases the difficulty to extract the useful signals from the useless noise. More rigorous work needs to be done on well known igneous and metamorphic systems to fully calibrate the structural and textural features to make it a quantitative geospeedometer.

Acknowledgements The authors thank Professor Michael A. Carpenter of Cambridge University for providing some of the samples studied in this work. We thank Ms. Vickie E. Lynch for her help with reducing the neutron diffraction data from modulated structures.

Funding information The following funding is acknowledged: National Science Foundation (grant No. EAR-1530614 to Huifang Xu, Dane Morgan). The neutron single-crystal diffraction measurement carried out at the Spallation Neutron Source was sponsored by the Division of Scientific User Facilities, Office of Basic Energy Sciences, US Department of Energy, under contract No. DE-AC05-00OR22725 with UT-Battelle, LLC. This study was also supported by the ORNL Graduate Opportunity (GO) Program.

References

- Angel, R. J., Carpenter, M. A. & Finger, L. W. (1990). *Am. Mineral.* **75**, 150–162.
- Arnold, O., Bilheux, J. C., Borreguero, J. M., Buts, A., Campbell, S. I., Chapon, L., Doucet, M., Draper, N., Ferraz Leal, R., Gigg, M. A., Lynch, V. E., Markvardsen, A., Mikkelsen, D. J., Mikkelsen, R. L., Miller, R., Palmen, K., Parker, P., Passos, G., Perring, T. G., Peterson, P. F., Ren, S., Reuter, M. A., Savici, A. T., Taylor, J. W., Taylor, R. J., Tolchenov, R., Zhou, W. & Zikovskiy, J. (2014). *Nucl. Instrum. Methods Phys. Res. Sect. Accel. Spectrometers Detect. Assoc. Equip.* **764**, 156–166.
- Bogdanova, S. V., Pashkevich, I. K., Buryanov, V. B., Makarenko, I. B., Orlyuk, M. I., Skobelev, V. M., Starostenko, V. I. & Legostaeva, O. V. (2004). *Eur. GeoRift 3 Intraplate Tecton. Basin Dyn. Lithosphere South. East. Eur. Craton Its Margin.* **381**, 5–27.
- Boysen, H. & Kek, S. (2015). *Z. Krist.* **230**, 23–36.
- Carpenter, M. A. (1986). *Phys. Chem. Miner.* **13**, 119–139.
- Carpenter, M. A. (1994). *Feldspars and Their Reactions*, Vol. 421, edited by Ian Parsons, pp. 221–269. Dordrecht: Kluwer Academic Publishers.
- Carpenter, M. A. & McConnell, J. D. C. (1984). *Am. Mineral.* **69**, 112–121.
- Carpenter, M. A., McConnell, J. D. C. & Navrotsky, A. (1985). *Geochim. Cosmochim. Acta.* **49**, 947–966.
- Ganguly, J. & Domeneghetti, M. C. (1996). *Contrib. Mineral. Petrol.* **122**, 359–367.
- Grove, T. L. (1982). *Am. Mineral.* **67**, 251–268.
- Grove, T. L., Baker, M. B. & Kinzler, R. J. (1984). *Geochim. Cosmochim. Acta.* **48**, 2113–2121.
- Gutmann, M. J., Petříček, V., Daoud-Aladine, M. A. & Martin, C. Y. (2008). *Meas. Sci. Technol.* **19**, 034005
- Holness, M. B., Tegner, C., Nielsen, T. F. D., Stripp, G. & Morse, S. A. (2007). *J. Petrol.* **48**, 2359–2377.
- Horst, W., Tagai, T., Korekawa, M. & Jagodzinski, H. (1981). *Z. Krist.* **157**, 233–250.
- Jin, S., Wang, X. P. & Lynch, V. E. (2019) Data reduction for single-crystal neutron diffraction on (3+d) dimension modulated structure with Mantid,
<https://docs.mantidproject.org/nightly/concepts/ModulatedStructure.html>
- Jin, S., Wang, X. P. & Xu, H. (2018). *Acta Crystallogr. Sect. B-Struct. Sci. Cryst. Eng. Mater.* **74**, 152–164.

- Jin, S. & Xu, H. (2017*a*). *Acta Crystallogr. Sect. B.* **73**, 992–1006.
- Jin, S. & Xu, H. (2017*b*). *Am. Mineral.* **102**, 21–32.
- Jin, S. & Xu, H. (2017*c*). *Am. Mineral.* **102**, 1328–1339.
- Jin, S., Xu, H., Wang, X. P., Zhang, D., Jacobs, R. & Morgan, D. (2019). *Acta Crystallogr. Sect. B-Struct. Sci. Cryst. Eng. Mater.* **75**, 643–656.
- Kroll, H. & Ribbe, P. H. (1983). *Feldspar Mineralogy*, Vol. 2, edited by P.H. Ribbe, pp. 57–100. Washington, D.C.: Mineralogical Society of American.
- McConnell, J. D. C. (1974). *The Feldspars*, Vol. edited by W.S. MacKenzie & J. Zussman, pp. 460–477. New York: Manchester University Press.
- McLaren, A. C. (1974). *The Feldspars*, Vol. edited by W.S. MacKenzie & J. Zussman, pp. 378–423. New York: Manchester University Press.
- Miller, J. D. (2009). *Precambrian Res. Cent. Guideb.* 1–23.
- Miller, J. D. & Weiblen, P. W. (1990). *J. Petrol.* **31**, 295–339.
- Momma, K. & Izumi, F. (2011). *J. Appl. Crystallogr.* **44**, 1272–1276.
- Nord Jr, G. L., Heuer, A. H. & Lally, J. S. (1974). *The Feldspars*, Vol. edited by W.S. MacKenzie & J. Zussman, pp. 522–535. New York: Manchester University Press.
- Petříček, V., Dušek, M. & Palatinus, L. (2014). *Z. Krist.* **229**, 345–352.
- Phillips, E. R., Chenhall, B. E., Stone, I. J. & Pemberton, J. W. (1977). *Mineral. Mag.* **41**, 469–471.
- Ribbe, P. H. (1983). *Feldspar Mineralogy*, Vol. 2, edited by P.H. Ribbe, pp. 241–270. Washington, D.C.: Mineralogical Society of American.
- Schultz, A. J., Jorgensen, M. R. V., Wang, X. P., Mikkelson, R. L., Mikkelson, D. J., Lynch, V. E., Peterson, P. F., Green, M. L. & Hoffmann, C. M. (2014). *J. Appl. Crystallogr.* **47**, 915–921.
- Schultz, A. J., Srinivasan, K., Teller, R. G., Williams, J. M. & Lukehart, C. M. (1984). *J. Am. Chem. Soc.* **106**, 999–1003.
- Smith, J. V. (1984). *Feldspars and Feldspathoids*, Vol. 137, edited by W.L. Brown, pp. 55–94. Dordrecht: Reidel Publishing Company.
- Smith, J. V. & Brown, W. L. (1988). *Feldspar Minerals* Berlin Heidelberg: Springer-Verlag.
- Toman, K. & Frueh, A. (1973*a*). *Z. Krist.* **138**, 337–342.
- Toman, K. & Frueh, A. J. (1971). *Acta Crystallogr. Sect. B.* **27**, 2182–2186.

- Toman, K. & Frueh, A. J. (1972). *Acta Crystallogr. Sect. B-Struct. Crystallogr. Cryst. Chem.* **28**, 1657-1662.
- Toman, K. & Frueh, A. J. (1973*b*). *Acta Crystallogr. Sect. A.* **29**, 127–133.
- Toman, K. & Frueh, A. J. (1973*c*). *Acta Crystallogr. Sect. A.* **29**, 121–127.
- Toman, K. & Frueh, A. J. (1976*a*). *Acta Crystallogr. Sect. B.* **32**, 521-525.
- Toman, K. & Frueh, A. J. (1976*b*). *Acta Crystallogr. Sect. B.* **32**, 526–538.
- Xu, H. (2015). *Am. Mineral.* **100**, 510–515.
- Yamamoto, A., Nakazawa, H., Kitamura, M. & Morimoto, N. (1984). *Acta Crystallogr. Sect. B-Struct. Sci.* **40**, 228–237.
- Zikovsky, J., Peterson, P. F., Wang, X. P., Frost, M. & Hoffmann, C. (2011). *J. Appl. Crystallogr.* **44**, 418–423.

Supporting information

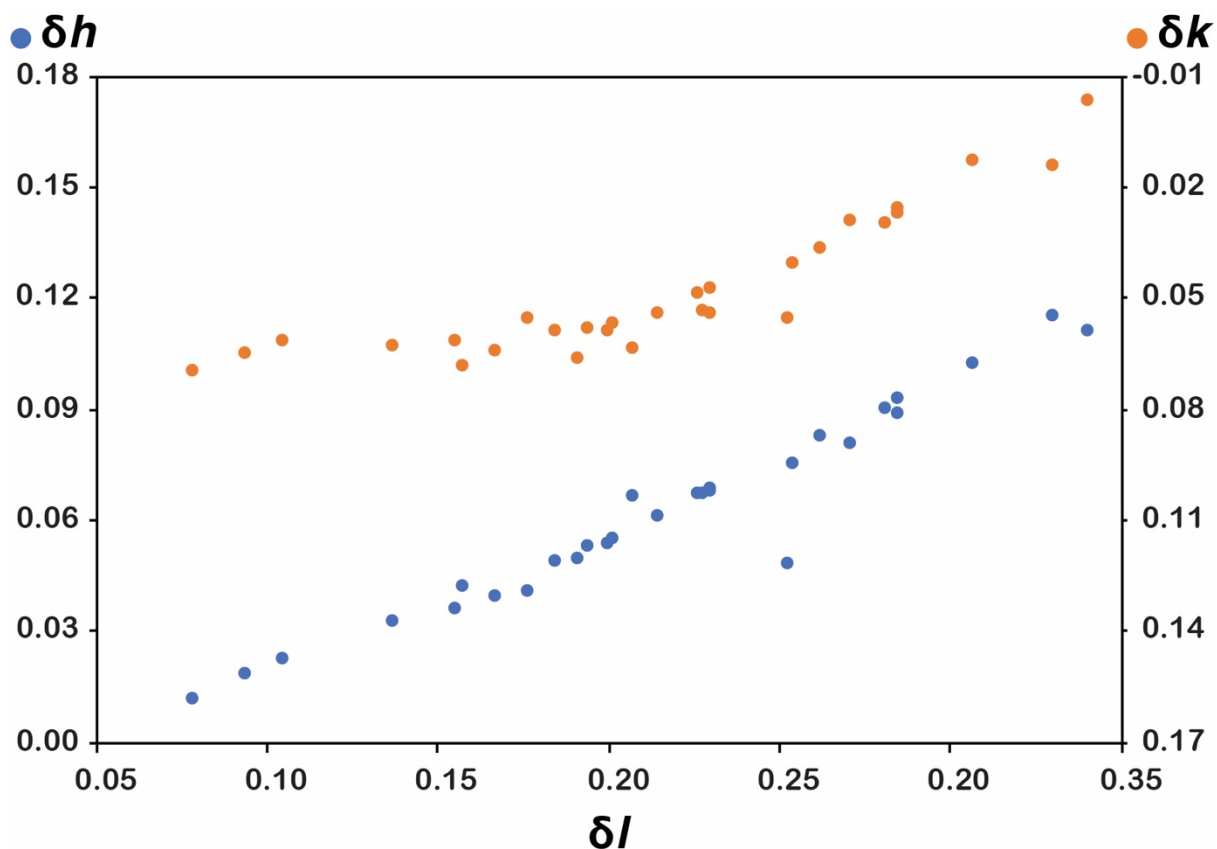


Figure S1 The δh and δk of the q -vector plotted against δl as in Smith & Brown (1988). This plot eliminates the error from the compositional analysis and shows strong correlation between the three components of the q -vectors. The points that obviously deviate from the trend are from volcanic samples with diffuse satellite reflections (Jin, Xu *et al.*, 2019).

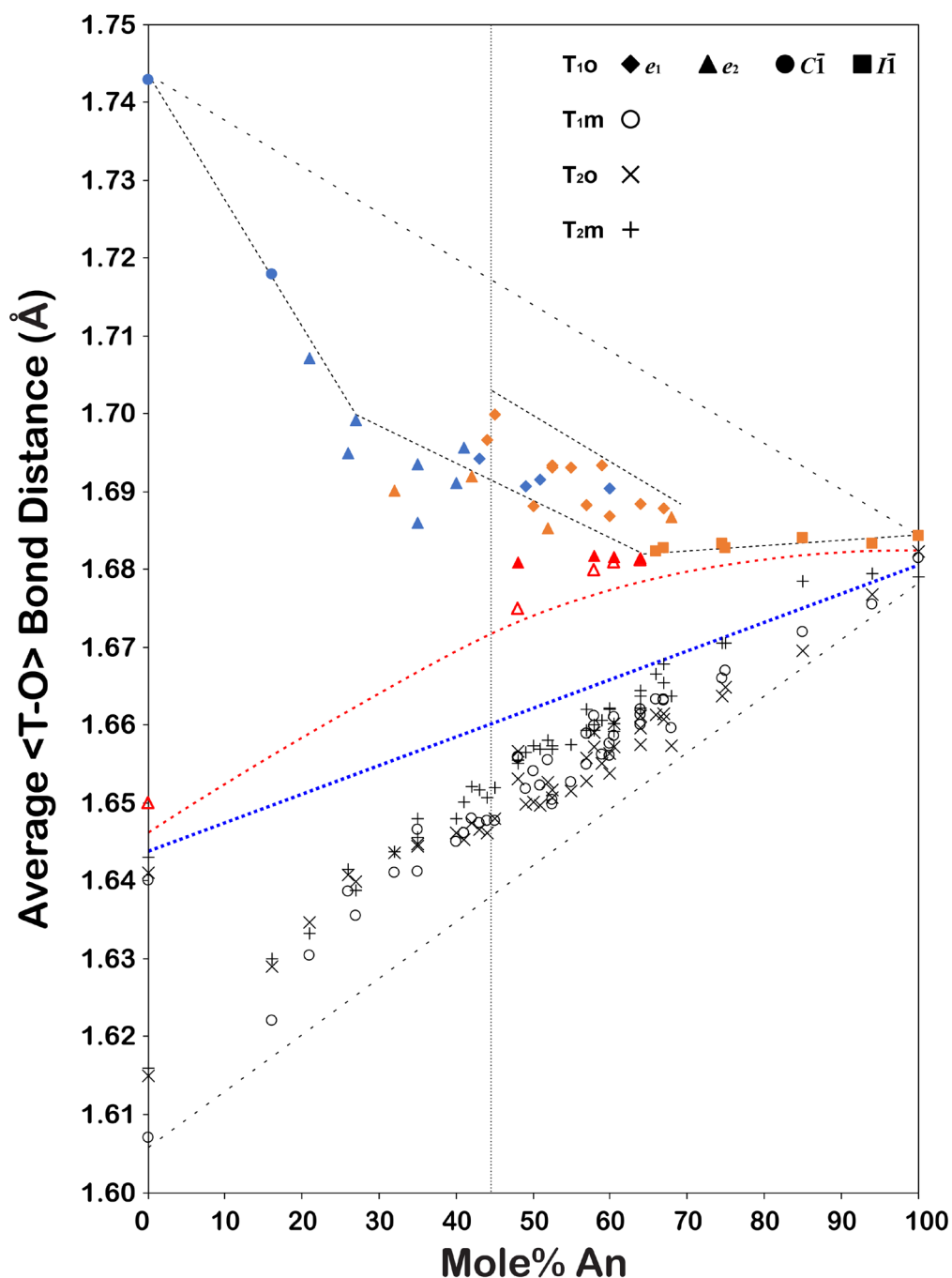


Figure S2 Average $\langle T-O \rangle$ bond distances of samples in this paper and several previously published papers (Jin & Xu, 2017*a,b,c*; Jin, Wang *et al.*, 2018; Jin, Xu *et al.*, 2019). Data points less calcic than An_{20} or more calcic than An_{75} are from Kroll & Ribbe (1983). The points for $\langle T_{1o}-O \rangle$ are color and shape coded based on their structure and origin. For two samples with the same composition, the one with less ordered structure is shifted slightly to the left to be discernible. The blue dotted line shows the regression of the total average $\langle T-O \rangle$ distance in each structure. The black dash lines outline the boundaries of the e_1 and e_2 structures. The red dotted line shows the trend for volcanic and heated plagioclase structures.

Table S1 Electron microprobe analyses results

SAMPLE	Oxide Weight Percentage							Formula per 8 oxygen							
	SiO ₂	Al ₂ O ₃	FeO	CaO	Na ₂ O	K ₂ O	TOTAL	Si	Al	Fe	Ca	Na	K	Totals	
7147A	55.025	28.731	0.172	10.778	5.315	0.441	100.462	2.473	1.522	0.006	0.519	0.463	0.025	13.010	An _{51.5} Ab _{46.0} Or _{2.5}
	54.034	28.812	0.179	10.909	5.093	0.414	99.442	2.455	1.543	0.007	0.531	0.449	0.024	13.009	An _{52.9} Ab _{44.7} Or _{2.4}
	54.505	28.548	0.225	10.960	5.144	0.412	99.795	2.468	1.524	0.009	0.532	0.452	0.024	13.008	An _{52.8} Ab _{44.8} Or _{2.4}
	54.860	28.607	0.284	11.082	5.252	0.392	100.476	2.469	1.517	0.011	0.534	0.458	0.022	13.013	An _{52.6} Ab _{45.1} Or _{2.2}
	54.491	28.550	0.229	10.784	5.164	0.406	99.624	2.470	1.525	0.009	0.524	0.454	0.023	13.006	An _{52.3} Ab _{45.3} Or _{2.3}
	55.210	28.800	0.245	10.795	5.112	0.403	100.566	2.477	1.523	0.009	0.519	0.445	0.023	12.996	An _{52.6} Ab _{45.1} Or _{2.3}
Volga Blue yellow	53.905	29.147	0.445	11.014	4.895	0.484	99.890	2.441	1.556	0.017	0.534	0.430	0.028	13.006	An _{53.9} Ab _{43.3} Or _{2.8}
	54.115	28.896	0.211	11.330	4.866	0.470	99.887	2.450	1.542	0.008	0.550	0.427	0.027	13.005	An _{54.7} Ab _{42.5} Or _{2.7}
	53.773	29.156	0.472	11.255	4.783	0.459	99.899	2.435	1.556	0.018	0.546	0.420	0.027	13.002	An _{55.0} Ab _{42.3} Or _{2.7}
	54.324	28.802	0.223	11.299	4.814	0.429	99.891	2.458	1.536	0.008	0.548	0.422	0.025	12.996	An _{55.1} Ab _{42.5} Or _{2.5}
	53.485	29.280	0.334	11.529	4.632	0.424	99.684	2.429	1.567	0.013	0.561	0.408	0.025	13.003	An _{56.5} Ab _{41.1} Or _{2.5}
	54.076	29.059	0.172	11.171	4.754	0.539	99.770	2.449	1.551	0.007	0.542	0.417	0.031	12.998	An _{54.7} Ab _{42.1} Or _{3.1}
	53.892	28.896	0.277	11.403	4.692	0.481	99.641	2.447	1.546	0.011	0.555	0.413	0.028	12.999	An _{55.7} Ab _{41.5} Or _{2.8}
	53.503	29.211	0.512	11.305	4.649	0.545	99.726	2.428	1.563	0.019	0.550	0.409	0.032	13.001	An _{55.5} Ab _{41.3} Or _{3.2}
53.903	29.048	0.337	11.312	4.795	0.437	99.831	2.443	1.552	0.013	0.549	0.421	0.025	13.003	An _{55.2} Ab _{42.3} Or _{2.5}	
89GM97	52.935	29.150	0.485	11.581	4.544	0.428	99.122	2.419	1.570	0.019	0.567	0.403	0.025	13.001	An _{57.0} Ab _{40.5} Or _{2.5}
	51.720	28.366	0.505	11.385	4.235	0.428	96.639	2.424	1.567	0.020	0.572	0.385	0.026	12.993	An _{58.2} Ab _{39.2} Or _{2.6}
	53.273	28.723	0.472	11.154	4.908	0.475	99.005	2.433	1.546	0.018	0.546	0.435	0.028	13.005	An _{54.1} Ab _{43.1} Or _{2.7}
	53.772	29.259	0.462	11.386	4.722	0.462	100.062	2.433	1.560	0.017	0.552	0.414	0.027	13.004	An _{55.6} Ab _{41.7} Or _{2.7}
	52.837	29.528	0.723	11.892	4.439	0.403	99.823	2.404	1.583	0.027	0.580	0.392	0.023	13.010	An _{58.3} Ab _{39.4} Or _{2.4}
	52.264	29.601	0.592	11.762	4.545	0.426	99.191	2.392	1.597	0.023	0.577	0.403	0.025	13.016	An _{57.4} Ab _{40.1} Or _{2.5}

	52.902	29.045	0.505	11.841	4.530	0.433	99.255	2.416	1.563	0.019	0.579	0.401	0.025	13.004	An _{57.6} Ab _{39.9} Or _{2.5}
	52.713	29.719	0.492	11.712	4.393	0.400	99.429	2.403	1.597	0.019	0.572	0.388	0.023	13.002	An _{58.2} Ab _{39.5} Or _{2.4}
Volga Blue colourless	52.836	29.439	0.263	12.122	4.352	0.329	99.340	2.410	1.583	0.010	0.592	0.385	0.019	12.999	An _{59.5} Ab _{38.6} Or _{1.9}
	53.135	29.423	0.257	11.942	4.451	0.353	99.561	2.417	1.577	0.010	0.582	0.393	0.020	12.999	An _{58.5} Ab _{39.5} Or _{2.1}
	52.573	29.148	0.317	12.033	4.676	0.389	99.135	2.408	1.573	0.012	0.590	0.415	0.023	13.022	An _{57.4} Ab _{40.4} Or _{2.2}
	53.773	29.493	0.364	12.114	4.450	0.306	100.499	2.424	1.567	0.014	0.585	0.389	0.018	12.996	An _{59.0} Ab _{39.2} Or _{1.8}
	52.097	29.398	0.504	12.153	4.419	0.391	98.962	2.393	1.592	0.019	0.598	0.394	0.023	13.019	An _{59.0} Ab _{38.8} Or _{2.3}
	51.743	29.352	0.279	11.996	4.445	0.350	98.164	2.393	1.600	0.011	0.594	0.399	0.021	13.017	An _{58.6} Ab _{39.3} Or _{2.0}
Dul-15-6A	52.849	30.752	0.487	13.412	3.976	0.135	101.612	2.363	1.621	0.018	0.643	0.345	0.008	12.997	An _{64.6} Ab _{34.6} Or _{0.8}
	52.293	30.742	0.438	13.232	3.930	0.140	100.773	2.357	1.633	0.017	0.639	0.343	0.008	12.997	An _{64.5} Ab _{34.7} Or _{0.8}
	52.722	30.726	0.469	13.379	4.057	0.156	101.510	2.361	1.622	0.018	0.642	0.352	0.009	13.004	An _{64.0} Ab _{35.1} Or _{0.9}
	51.579	30.537	0.475	13.244	3.928	0.149	99.911	2.348	1.638	0.018	0.646	0.347	0.009	13.006	An _{64.5} Ab _{34.6} Or _{0.9}